

# LAMOST DR1: STELLAR PARAMETERS AND CHEMICAL ABUNDANCES WITH SP\_Ace

C. BOECHE

Astronomisches Rechen-Institut, Zentrum für Astronomie der Universität Heidelberg, Mönchhofstr. 12-14, 69120 Heidelberg, Germany  
 and  
 INAF, Padova Observatory, Vicolo dell'Osservatorio 5, 35122 Padova, Italy

M. C. SMITH

Key Laboratory for Research in Galaxies and Cosmology, Shanghai Astronomical Observatory, Chinese Academy of Sciences, 80  
 Nandan Road, Shanghai 200030, China

E. K. GREBEL

Astronomisches Rechen-Institut, Zentrum für Astronomie der Universität Heidelberg, Mönchhofstr. 12-14, 69120 Heidelberg, Germany

J. ZHONG

Key Laboratory for Research in Galaxies and Cosmology, Shanghai Astronomical Observatory, Chinese Academy of Sciences, 80  
 Nandan Road, Shanghai 200030, China

J.L. HOU

Key Laboratory for Research in Galaxies and Cosmology, Shanghai Astronomical Observatory, Chinese Academy of Sciences, 80  
 Nandan Road, Shanghai 200030, China and  
 University of Chinese Academy of Sciences, Beijing 100049, China

L. CHEN

Key Laboratory for Research in Galaxies and Cosmology, Shanghai Astronomical Observatory, Chinese Academy of Sciences, 80  
 Nandan Road, Shanghai 200030, China and  
 University of Chinese Academy of Sciences, Beijing 100049, China

AND

D. STELLO

School of Physics, University of New South Wales, NSW 2052, Australia  
 Sydney Institute for Astronomy (SIfA), School of Physics, University of Sydney, NSW 2006, Australia and  
 Stellar Astrophysics Centre, Department of Physics and Astronomy, Aarhus University, Ny Munkegade 120, DK-8000 Aarhus C,  
 Denmark

*Draft version February 16, 2022*

## ABSTRACT

We present a new analysis of the LAMOST DR1 survey spectral database performed with the code SP\_Ace, which provides the derived stellar parameters  $T_{\text{eff}}$ ,  $\log g$ ,  $[\text{Fe}/\text{H}]$ , and  $[\alpha/\text{Fe}]$  for 1 097 231 stellar objects. We tested the reliability of our results by comparing them to reference results from high spectral resolution surveys. The expected errors can be summarized as  $\sim 120$  K in  $T_{\text{eff}}$ ,  $\sim 0.2$  in  $\log g$ ,  $\sim 0.15$  dex in  $[\text{Fe}/\text{H}]$ , and  $\sim 0.1$  dex in  $[\alpha/\text{Fe}]$  for spectra with  $\text{S/N} > 40$ , with some differences between dwarf and giant stars. SP\_Ace provides error estimations consistent with the discrepancies observed between derived and reference parameters. Some systematic errors are identified and discussed. The resulting catalog is publicly available at the LAMOST and CDS websites.

*Keywords:* catalogs — surveys

## 1. INTRODUCTION

During the last decades the formation and evolution of the Milky Way (MW) has become a question of major importance in modern astrophysics. The proximity of our Galaxy permits individual star-by-star investigations that would not be possible for external galaxies. This opportunity has been grasped by many research groups who have planned and run spectroscopic surveys of the MW at high- and low-spectral resolution (e.g., the Apache Point Observatory Galactic Evolution Experiment, APOGEE, Allende Prieto et al. 2008; the

Galactic Archaeology with HERMES (GALAH) Survey, Zucker et al. 2012; the Gaia-ESO Public Spectroscopic Survey, Gilmore et al. 2012; the Sloan Extension for Galactic Understanding and Exploration, SEGUE, Yanny et al., 2009; the RAdial Velocity Experiment, RAVE, Steinmetz et al. 2006; the 4-Metre multi-Object Spectroscopic Telescope, 4MOST, de Jong et al. 2012; the WHT Enhanced Area Velocity Explorer, WEAVE, Dalton et al. 2012).

While high-resolution spectroscopy can provide higher accuracy in stellar parameters and chemical abundances for relatively small samples of stars that are relatively bright (e.g.  $10^6$  stars brighter than  $V=14$  for GALAH),

low-resolution spectroscopy is better suited to collecting spectra of stars of fainter magnitude, thus securing a much larger sample ( $25 \cdot 10^6$  stars down to  $V=20$  for 4MOST).

The Large Sky Area Multi-Object Fiber Spectroscopic Telescope (LAMOST, Cui et al. 2012) is a telescope with effective aperture of 4m, which is used to conduct Galactic and extra-galactic spectroscopic surveys at spectral resolution of  $R \sim 2000$ . The LAMOST Experiment for Galactic Understanding and Exploration (LEGUE, Deng et al., 2012) is an on-going Galactic survey that, with a present sample of more than 5 million stellar spectra of the MW, is the largest spectroscopic survey available to the astronomical community. The first data release (DR1, Luo et al. 2015) includes 2 204 696 spectra, of which 1 944 329 are spectra of stars in the MW (corresponding to around 1.6M unique stars). Public data releases have followed on an annual basis<sup>1</sup>.

In our current paper we present the stellar parameters and chemical abundances obtained by applying the code SP\_Ace (Boeche & Grebel, 2016, see also Section 3) to the LAMOST DR1 spectra. Stellar parameters, such as  $T_{\text{eff}}$ ,  $\log g$ , and  $[M/H]$  have already been derived, most notably by the official LAMOST pipeline, LASP (Luo et al., 2015). This pipeline initially compares the observed spectra to a library of synthetic spectra derived from a Kurucz/ATLAS9 grid in order to obtain a first, coarse, estimate of the parameters. After this the *ULySS* method (Koleva et al. 2009, Wu et al. 2011), using the ELODIE spectral library (Prugniel et al. 2007) for the template spectra, is applied. In addition to LASP, other groups have carried out their own analyses. Ho et al. (2017a, 2017b) have applied a method based on the “The Cannon” (Ness et al., 2015), which estimates parameters by training a model on existing data sets (in this instance from the APOGEE survey). From this analysis they are able to deriving parameters for giant stars, including  $[\alpha/\text{Fe}]$ , individual  $[C/M]$  and  $[N/M]$  abundances and, from these latter two abundances, masses and ages. Xiang et al. (2015) present another analysis, like LASP also matching to template spectra (in this case observed libraries from MILES and ELODIE). A recent update to this pipeline now delivers alpha-element abundances and, by applying a machine learning algorithm to the giant stars,  $[C/N]$  and  $[N/H]$  abundances (Xiang et al. 2017). By using SP\_Ace we derive the stellar parameters  $T_{\text{eff}}$ ,  $\log g$ ,  $[\text{Fe}/H]$ , and the alpha abundances  $[\alpha/\text{Fe}]$  for both dwarf and giant stars.

## 2. DATA

We employ the LAMOST spectra from the first data release (DR1, Luo et al., 2015) using the latest internal DR3 reduction. Out of the 2 204 969 spectra belonging to the DR1 catalog, 1 944 329 were classified as stars, the rest as galaxies, quasars, or other non-stellar objects. These spectra are radial velocity corrected for the Earth motion (only), flux calibrated, and are the result of joining the two spectra obtained by the blue and red arms of the spectrographs (Luo et al., 2015). The spectra are re-binned to a constant velocity dispersion so that the pixel interval is constant in

$\log \lambda$ . The calibration is in the vacuum wavelength. To process these spectra with SP\_Ace and derive stellar parameters and chemical abundances we must re-shape the spectra by: i) converting the dispersion from  $\log \lambda$  to  $\lambda$  (angstrom), ii) converting the wavelength from vacuum to air, and iii) normalizing the flux. We used the IRAF<sup>2</sup> task *disptans* to convert the wavelength calibration from vacuum to air and from  $\log \lambda$  to  $\lambda$ . This conversion renders a spectral dispersion that is not constant. To flux normalize the spectra we used the IRAF task *continuum* with the settings

*function=spline3 order=3 low\_rej=1 high\_rej=3 nitrat=5.*

Out of the 2 204 969 DR1 spectra, we processed 2 052 662 spectra; 152 300 were not present in the internal DR3 catalog, mostly objects with low ( $< 20$ ) signal-to-noise ratio (S/N), while 7 spectra failed the IRAF tasks described above. We ran all of the spectra through SP\_Ace, including the ones classified as non-stellar objects to cover possible mis-classifications. Because SP\_Ace was designed for stellar spectra, we expect no convergence (and therefore null values to be output) for spectra of objects that are not stars (this is discussed in Section 3.3).

## 3. THE SP\_Ace CODE

The SP\_Ace software (Boeche & Grebel, 2016) derives stellar parameters and chemical abundances of FGK stars from the analysis of their spectra in the wavelength windows 5212-6960Å and 8400-8920Å. The software uses a novel method to derive these parameters. Many pipelines rely on equivalent width (*EW*) measurements (among others, Fast Automatic Moog Analysis, FAMA, Magrini et al. 2013; GALA, Mucciarelli et al. 2013) or on libraries of synthetic spectra (among others, the MATrix Inversion for Spectral Synthesis, MATISSE, Recio-Blanco et al. 2006; FERRE, Allende Prieto et al. 2006), while others rely on training sets of standard stars (The Cannon, Ness et al. 2015; ULySS, Koleva et al. 2009; LASP, Luo et al. 2015). Unlike these, SP\_Ace relies on a library of general curves-of-growth (GCOG). The GCOG is a function that describes the *EW* of an absorption line as a function of the stellar parameters  $T_{\text{eff}}$ ,  $\log g$ , and  $[\text{El}/H]$ , where “El” is the element the line belongs to. The GCOG is, therefore, the generalization of the classical curve-of-growth extended to the parameters  $T_{\text{eff}}$  and  $\log g$ . Given the stellar parameters  $T_{\text{eff}}$ ,  $\log g$ , and the abundances  $[\text{El}/H]$ , SP\_Ace takes the GCOG of the lines stored in the GCOG library for the wavelength interval under consideration and computes the expected *EW*s. Then, assuming a Voigt line profile, SP\_Ace constructs a model spectrum by subtracting these line profiles (with the just-computed *EW*s) from a continuum normalized to 1. This is described in more detail in section 7.1 of Boeche & Grebel 2016 (see also Fig. 1 of the current paper). In this way SP\_Ace constructs many model spectra of different stellar parameters and searches for the one that minimizes the  $\chi^2$  between the observed and the model spectrum. The  $\chi^2$  is minimized following the Levenberg-Marquadt method, details of which are

<sup>1</sup> <http://www.lamost.org>

<sup>2</sup> Image Reduction and Analysis Facility, <http://iraf.noao.edu>.

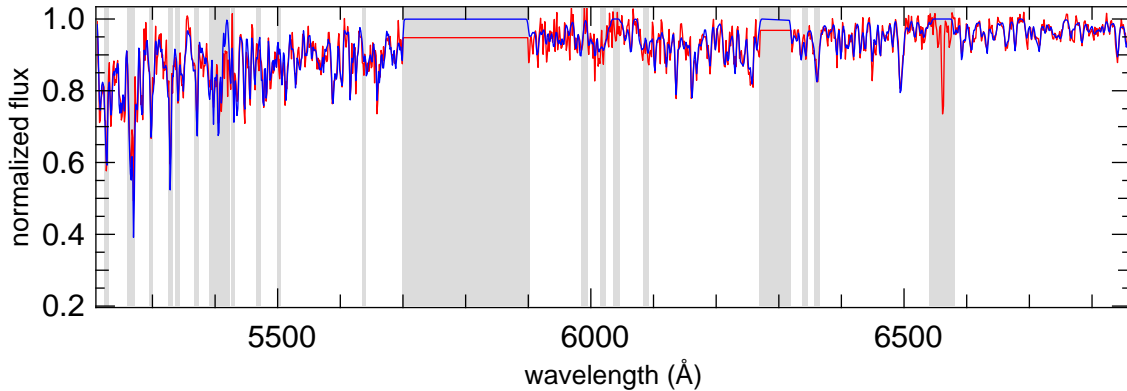


**Figure 1.** LAMOST spectrum spec-55932-GAC\_061N46\_V1\_sp03-061 (in red) and the best matching model found by SP\_Ace (in blue) with derived parameters of  $T_{\text{eff}}=4642$  K,  $\log g=2.60$ ,  $[M/H]=0.24$  dex. The observed spectrum has  $S/N=44$  and it has been continuum re-normalized with the internal SP\_Ace procedure. Shaded areas are the rejected wavelength intervals.

given in section 7.3 of Boeche & Grebel (2016). This method of comparing model spectra and observed spectra puts SP\_Ace in the “global fitting methods” category. We remind the reader that as input SP\_Ace takes spectra that have been wavelength calibrated, radial velocity corrected to the rest frame, and continuum normalized. However, SP\_Ace can apply changes in radial velocity (RV) to the model spectrum (see section 7.3 of the Boeche & Grebel 2016 paper). This feature was implemented in the code because experience showed that SP\_Ace could detect small wavelength shifts in observed spectra, even when these were previously RV corrected to the rest frame. Since this can badly affect the  $\chi^2$  analysis, we allowed SP\_Ace to perform small shifts (no larger than  $\sim 1$  FWHM) to the spectrum model. This was supposed to be a mere internal setting performed in order to better match the observed spectrum and increase the accuracy of the derived stellar parameters. In fact, in the case of high resolution spectra, a shift of 1 FWHM in wavelength corresponds to a small shift in RV (at  $R \sim 20\,000$  this corresponds to  $\sim 15$  km s $^{-1}$ ). The case of low resolution spectra (like LAMOST) is different, because a 1 FWHM shift corresponds to  $\sim 200$  km s $^{-1}$  in RV. Because the LAMOST spectra are corrected for the Earth’s motion only, these internal RV corrections correspond to the heliocentric RVs of the LAMOST stars. From now on, we refer to these shifts as the SP\_Ace RV corrections. However, SP\_Ace was not designed to measure RVs and has never been tested for this purpose, therefore will not use them as such. Official LAMOST RVs have been determined by the LAMOST 1D pipeline (see Luo et al 2015).

Similarly, SP\_Ace applies a continuum re-normalization to the (already normalized) observed spectra as an internal trim of the continuum to improve the  $\chi^2$  analysis. This internal setting was implemented because the normalization of spectra (done with IRAF or similar tools) are often not optimal in the case of wide absorption lines and/or high metallicity. This is due to the difficulty in distinguishing the continuum level from a pseudo-continuum generated by the wide blends of lines or wings of wide strong lines. However, in order to deal with certain idiosyncrasies of the LAMOST spectra, we have changed some parts of the code, as explained in the following section.

### 3.1. The LAMOST version of SP\_Ace

To fully exploit the information carried by the LAMOST spectra we need to consider the largest wavelength range possible. This means that both the blue and red parts of the spectra must be used for the analysis. However, the blue and red parts differ from each other as follows:

- Spectral dispersions: The LAMOST spectra have been rebinned to a wavelength width that is constant in  $\log \lambda$ . This means that the binning in wavelength (employed by SP\_Ace) varies along the whole spectrum.
- S/N: The intensity of the blue and the red parts of a spectrum change not only as a function of the temperature of the stars, but also because the efficiency of the two spectrograph arms differs. Therefore the S/N of these two parts is different. Furthermore the S/N changes inside each of the two parts because the central part of the spectral orders receives more light than the borders (blaze function).
- Spectral resolutions: The instrumental full-width-half-maximum (FWHM) of the blue and red arm of the spectroscope differ, with the former being smaller than the latter.
- Wavelength calibration: There are differences in the wavelength calibration between the blue and red parts of the spectra, since they are done independently. This can lead to small differences in RV.

The most recent public version of SP\_Ace is able to handle spectra with a dispersion and S/N varying along the spectrum. However, for the analysis of a given spectrum, the public version of SP\_Ace assumes one single FWHM and radial velocity correction. This makes the public version of SP\_Ace unsuitable for a full exploitation of the LAMOST spectra. To overcome this limitation, we have made a custom version of SP\_Ace capable of analyzing the blue and red parts of the spectra separately. This version estimates an individual radial velocity correction and instrumental FWHM for each of the two parts, while simultaneously searching for a single set of stellar parameters and chemical abundances with a unique  $\chi^2$  analysis. Unlike the public version of

SP\_Ace, this version also makes use of the H $\alpha$  absorption line because it improves the parameter estimation of the LAMOST spectra for dwarf stars. For giant stars deviations from local thermodynamic equilibrium (non-LTE) can affect H $\alpha$  significantly, but for dwarf stars (i.e., stars with high gravities,  $\log g > 4$ ) the LTE assumptions are good enough to predict a reliable strength for this line. Therefore, the LAMOST version of SP\_Ace uses this line by assigning different weights to the pixels associated with the line<sup>3</sup> as follows,

$$\begin{aligned} \text{weight} &= 1 && \text{for } \log g \geq 4 \\ \text{weight} &= 1 - (4 - \log g) && \text{for } 3 < \log g < 4 \\ \text{weight} &= 0 && \text{for } \log g \leq 3. \end{aligned} \quad (1)$$

This provides a significant improvement in  $\log g$  for dwarf stars, while leaving the analysis of giant stars unaffected. For this work only, the H $\alpha$  GCOG employed has been obtained with the same procedure followed for the other lines, but we used the spectrum synthesis code SPECTRUM (Gray & Corbally, 1994) instead of MOOG (Snedden 1973). This was done because, with the same atomic parameters and stellar atmospheres employed as for the official SP\_Ace GCOG library, the strength of the H $\alpha$  line synthesized with SPECTRUM is bigger than the one in MOOG and it provides a better match to that of the Sun and Procyon. For this line only, we adopted the approximated Voigt profile by Bruce et al. (2000),

$$\text{Voigt}(x) = EW \cdot [rL(x) + (1-r)G(x)], \quad (2)$$

where  $L$  and  $G$  are the Lorentzian and Gaussian functions and  $EW$  is the equivalent width expressed in Å. While the FWHM of the Gaussian is equal to the spectral resolution FWHM (one of the variables that SP\_Ace actively looks for), the  $\sigma$  of the Lorentzian profile depends on the  $EW$  according to the following relation,

$$\sigma_L = EW \cdot \left(1 - \exp(-(2EW)^2)\right) \quad (3)$$

where  $\sigma_L$  is expressed in Å, and the  $r$  parameter in equation 2 is defined as,

$$r = \frac{1}{\exp\left(\frac{1\text{Å}}{2EW+0.001}\right)}. \quad (4)$$

These are empirical relations that have been chosen to provide an optimal match to the observed H $\alpha$  line profile.

Although the LAMOST catalog provides an estimate of the error on the flux of a spectrum (inverse variance), it has been noted that this overestimates the true uncertainty (e.g., Ho et al. 2017a, Xiang et al. 2015). If we use these values in our fitting this will result in unreliable parameter uncertainties and so we have chosen to estimate the error ourselves. The uncertainty on the  $i$ -th pixel is taken as the standard deviation of the residuals computed over an interval with 25 pixels of half-width and centered on the  $i$ -th pixel (after the pixels deviating more than  $3\sigma$  were rejected). This approach ensures that the

best-fit reduced  $\chi^2$  is approximately one for most spectra and hence the parameter uncertainties should be reliable.

With this version of SP\_Ace we processed the 2 052 662 LAMOST DR1 stellar spectra, along with more than 50 000 spectra from later data releases. This latter sample consists of spectra of stars with existing stellar parameters in the literature, chosen so that we can validate our results (see Section 4). We limited the analysis to the wavelength intervals 5212–5700Å, 5900–6270Å, and 6320–6860Å. The first neglected interval (5700–5900Å) avoids the overlapping region of the blue and red arm, while the second one (6270–6320Å) avoids the region affected by telluric lines. The processing was carried out with the SP\_Ace options “ABD\_loop” and “alpha” switched on. The first option forces SP\_Ace to estimate the stellar parameters and chemical abundances using a loop, whereby the stellar parameters are derived again using the last abundance estimation, and vice versa, until they reach convergence. The second option imposes that the absorption lines of the elements Mg, Si, Ca, and Ti must be derived as if they were one single element called the  $\alpha$ -element<sup>4</sup> by forcing the relative abundances of these elements to be equal to each other. Similarly, all of the other non- $\alpha$  elements are derived as though they were the same element that we call “Fe”. Although this may appear imprecise, this parameter traces more closely Fe than the other elements because most of the absorption lines that drive it are in fact iron lines. The choice of grouping alpha elements and heavy elements together is due to the features of our spectra. A good fraction of the LAMOST spectra have low signal-to-noise and their low spectral resolution does not allow individual fit for most of the absorption lines. By grouping together absorption lines for similarly behaving elements, the total absorbed flux is bigger than for the individual elements and so it makes detectability easier in low signal-to-noise spectra. The “lack of purity” for the  $\alpha$ - and Fe-abundance is the price we pay to obtain abundance measurements for a higher number of spectra and with greater precision.

### 3.2. Complementary parameters

The first few columns of the SP\_Ace output report some parameters that, although usually not used for science, can be helpful in determining features and quality of the spectra. These parameters are as follows:

- **FWHM:** The standard SP\_Ace pipeline estimates only one FWHM for the whole spectrum. Because LAMOST spectra are actually composed of two separate spectra (the blue and the red part), which have different spectral resolutions, the LAMOST version of SP\_Ace estimates FWHMs for the blue and the red spectrum parts independently. These are output as FWHMb and FWHMr, respectively. The FWHMb and FWHMr differ and their values are (on average)  $\sim 2.9$  and  $\sim 4.3$ Å, respectively (see top panel of Fig. 2). Only  $\sim 2\%$  of the spectra have FWHMb  $> 4$ Å and  $\sim 3\%$  have FWHMr  $> 6$ Å. These values may be used as quality selection criteria, although we do not adopt any such cuts in this study

<sup>3</sup> We classify pixels as belonging to the H $\alpha$  line if they are within  $3\sigma$  of the centre of the line, where we assume that the line profile is approximately Gaussian (i.e.  $1 \text{ FWHM} = 2.35\sigma$ ).

<sup>4</sup> Other  $\alpha$  elements, such as O and S, are not considered here because these are among the elements whose abundances derived by SP\_Ace are (to date) considered not reliable.



as the number of stars with very high FWHM is negligible. Spectra with unusually large FWHM may be out-of-focus spectra, fast rotator stars, or have bad seeing, for which we do not expect reliable parameter estimations. As expected, the two FWHMs are weakly correlated, meaning that if the FWHM is large in the blue arm then there is a tendency for it to be large for the red arm as well.

- **Radial Velocity:** Like the FWHM, the radial velocity correction is also independently estimated for the blue and the red parts of the spectrum (RVb and RVr, respectively). Note that SP\_Ace was designed to take radial velocity corrected spectra and, in the case of small errors in the wavelength calibration or RV correction, it can correct for this by shifting the central wavelengths of the lines in the model spectrum. The limit of this shift is  $1.27\text{FWHM}$ , which is equivalent to a  $3\sigma$  shift for a Gaussian profile; this limit corresponds to an RV offset of  $\sim \pm 200 \text{ km s}^{-1}$  for an average  $\text{FWHMb}=2.9\text{\AA}$ . Because the FWHM varies for different spectra, the RV correction limit varies as well.<sup>5</sup> For stars having a RV that causes a wavelength shift larger than  $1.27 \text{ FWHM}$ , SP\_Ace quits the analysis reports no results.

Since the LAMOST spectra are corrected for the Earth's motion only (i.e., they are in the heliocentric frame), the RV correction performed by SP\_Ace corresponds to the heliocentric RV of the star. This means that the RVb and RVr should agree to within their uncertainties. If the difference between RVb and RVr is large it may indicate a mis-calibration of the wavelength or an incorrect RV convergence of SP\_Ace in one of the two parts of the spectrum. In the bottom panel of Fig. 2 the grey solid histogram shows the distribution of RVb minus RVr for the first full year of the survey.<sup>6</sup> This distribution is not symmetric and peaks at  $\sim -7 \text{ km s}^{-1}$ , which means that typical spectra have a value of RVr that is  $7 \text{ km s}^{-1}$  larger than RVb. This offset remains even if we select only high S/N spectra. The cause of this shift may be related to the  $5.7 \text{ km s}^{-1}$  difference between LAMOST and APOGEE radial velocities reported by Tian et al. 2014 (see section 2.3). If we compare our radial velocities to those from the LAMOST pipeline, we find that less than 0.5% of stars with  $\text{S/N} > 40$  have offsets greater than  $\pm 30 \text{ km s}^{-1}$ . From this we conclude that our stellar parameters are unlikely to be affected by problems with the radial velocity correction.

- **S/N:** This is a quality indicator of the spectra.

<sup>5</sup> While this work was in progress, we discovered a bug in the code which can cause the limit of the RV correction to change for different spectra. This is discussed in Appendix A. As a consequence of this bug some spectra will fail to converge, but the parameters reported in the catalog for the converged stars are unaffected.

<sup>6</sup> We found that there is a problem with LAMOST's radial velocity calibration for the red part of the spectra prior to MJD = 55945 and so here we only plot data from the first full year of the survey, i.e., from 29th Sept 2012. Note that the stellar parameters should be unaffected for these early spectra.

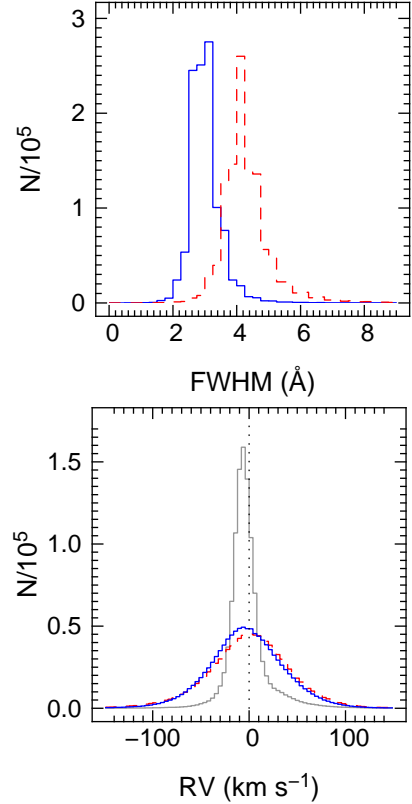


**Figure 2.** Top panel: The distribution of the FWHMs for the blue part (blue solid line) and the red part (red dashed line) of the spectra. Bottom panel: The distribution of radial velocities for the blue (RVb) and the red (RVr) part of the spectra (blue solid and red dashed histograms, respectively). The solid gray histogram represents the distribution of the difference RVb minus RVr. For this panel we have only plotted data from the first full year of the survey (see Section 3.2 for details).

As discussed above, each spectrum will have a S/N that varies with wavelength. SP\_Ace computes a pixel-by-pixel S/N based on the discrepancy between the observed spectrum and the best matching model, using a 50-pixel interval (25-pixel half-width) centered on the pixel under consideration. However, in its output SP\_Ace delivers a single value for the S/N. This is computed as  $\text{S/N}_{\text{SPAce}} = 1/\sigma_{\text{tot}}$ , where  $\sigma_{\text{tot}}$  is the standard deviation of the residuals between the observed spectrum and the best matching model over the whole spectrum, i.e., this can be considered as an average S/N<sup>7</sup>. In Fig. 3 we compare  $\text{S/N}_{\text{SPAce}}$  to the *I*-band signal-to-noise (SNRI) given in the LAMOST catalog, where we only include spectra that have stellar parameters in both catalogs. The two S/Ns show a fair 1:1 trend, although for some spectra the difference can be significant (note that the SNRI is evaluated in a wavelength window centered on  $6220\text{\AA}$ ). The peak of the S/N distribution is around 30, with the SP\_Ace distribution being slightly higher. This shift is probably due to the aforementioned issue

<sup>7</sup> Throughout this paper we use the term S/N to refer to the signal-to-noise as general meaning and the term  $\text{S/N}_{\text{SPAce}}$  to refer to the signal-to-noise derived by SP\_Ace. When we refer to the LAMOST signal-to-noise we use the quantity SNRI, which is calculated in the *I*-band.

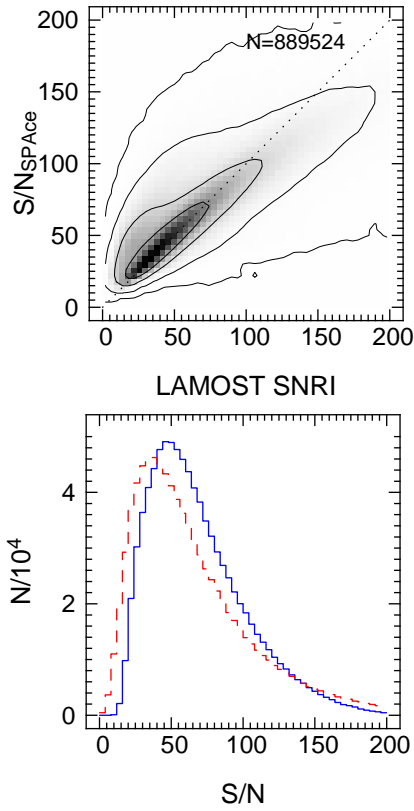


**Figure 3.** Top panel: 1:1 comparison between  $S/N_{\text{SP\_Ace}}$  and the LAMOST SNRI (S/N in the I band). Bottom panel: distributions of  $S/N_{\text{SP\_Ace}}$  (blue solid line) and LAMOST SNRI (red dashed line) for the spectra that have results in both catalogs. The contours enclose 34, 68, 95, and 99% of the sample.

regarding LAMOST’s flux error estimate (see Section 3.1). For lower S/N spectra one or both methods often fail to converge, mainly due to a lack of information in the spectra. Other issues that affect convergence are cosmetic defects (such as cosmic rays, fringing or dead pixels), emission lines, or any other peculiar/unexpected features, like non-stellar objects. As mentioned in the previous bullet point, SP\_Ace may also fail to converge if the radial velocity correction is too large. We return to the issue of performance later in Section 5.2 when we compare the results of SP\_Ace to those from the official LAMOST pipeline LASP.

### 3.3. Objects class discrimination

Although the majority of the LAMOST spectra processed with SP\_Ace are stellar objects, a fraction of the sample are non-stellar such as galaxies, quasars, planetary nebulae. Because SP\_Ace has been designed to derive stellar parameters of FGK stars only, it is expected not to converge (and to exit without results) for other objects. According to the LAMOST 1D pipeline’s classification (CLASS), 95% of our sample are stars. SP\_Ace converges for 56% of these, which is a similar success rate as for the LAMOST pipeline (58%), and most have good S/N (96% have  $S/N_{\text{SP\_Ace}} > 20$ ). On the other hand, from the 5% of spectra classified as non-stellar objects, SP\_Ace converges for about 1% of them (1331 objects). A by-eye inspection shows that these appear to be mostly bona fide stars, indicating that the LAMOST CLASS classifica-

tion is not perfect. Note that we are unable to determine the false-positive rate for CLASS, i.e., the fraction of non-stellar spectra that were classified as stars.

## 4. VALIDATION

To verify the reliability of the LAMOST stellar parameters and chemical abundances obtained with SP\_Ace we compared them against stars with stellar parameters in the literature. For these tests we restricted ourselves to LAMOST spectra with sufficient S/N to allow for a fair estimation of the chemical abundance, so we only selected stars with  $S/N_{\text{SP\_Ace}} > 40$ . We return to the issue of performance as a function of  $S/N_{\text{SP\_Ace}}$  later in Section 4.4.

### 4.1. Comparison to APOGEE

APOGEE (Holtzman et al. 2015) is a large spectroscopic survey that has collected over  $\sim 150,000$  spectra in the near infrared with a spectral resolution of  $\sim 22,500$ . The APOGEE stellar parameters and chemical abundances are derived with the APOGEE Stellar Parameters and Chemical Abundances Pipeline (ASPCAP; García Pérez et al. 2016), which compares the observed spectra to libraries of theoretical spectra and then calibrates the resulting parameters and abundances using an observed calibration sample. Although method and data are different from LAMOST’s, the comparison is useful. The complete DR12 APOGEE sample has 34 783 stars in common with LAMOST (45 193 LAMOST spectra, including repeat observations). Out of these spectra, we ignored the 27 021 spectra which are flagged by APOGEE as having possible problems in the spectrum (for instance, the stars may have a bright neighbor that can pollute the spectrum, particularly broad lines or low S/N that can badly affect the parameter derivation)<sup>8</sup>. This left us with 18 172 stellar spectra that have no reported problems, of which 13 351 are giant stars ( $\log g < 3.5$ ) with calibrated stellar parameters. We neglect the dwarf stars because APOGEE does not provide reliable parameters for these stars (Holtzman et al., 2015). SP\_Ace converged for 10 879 spectra of those giant stars, of which 9 189 had  $S/N_{\text{SP\_Ace}}$  above our aforementioned threshold of 40.

The performance of the two catalogs is shown in Fig. 4. The top panels show the  $(T_{\text{eff}}, \log g)$  plane, together with a set of fiducial isochrones by Bressan et al. (2012) corresponding to typical thin-disc, thick-disc and halo populations. SP\_Ace provides a good match to the expected distribution, as demonstrated by the agreement with the isochrones. In the bottom panels of Fig. 4 we directly compare the SP\_Ace and APOGEE stellar parameters, while a more detailed plot showing the correlations between the parameters is given in the Appendix B (Fig. 17). Since APOGEE gravities are calibrated using asteroseismic gravities from Kepler, we defer the discussion of the gravity performance to the following section where we directly compare to data from Kepler (Section 4.2). The distributions show some systematic differences (shifts and/or correlations) between APOGEE

<sup>8</sup> In our APOGEE sample all the spectra having  $[\text{Fe}/\text{H}] < -0.6$  dex were flagged as problematic by Holtzman et al. during their abundance estimation. Since we wish to retain the comparison with these stars we neglected such flags.

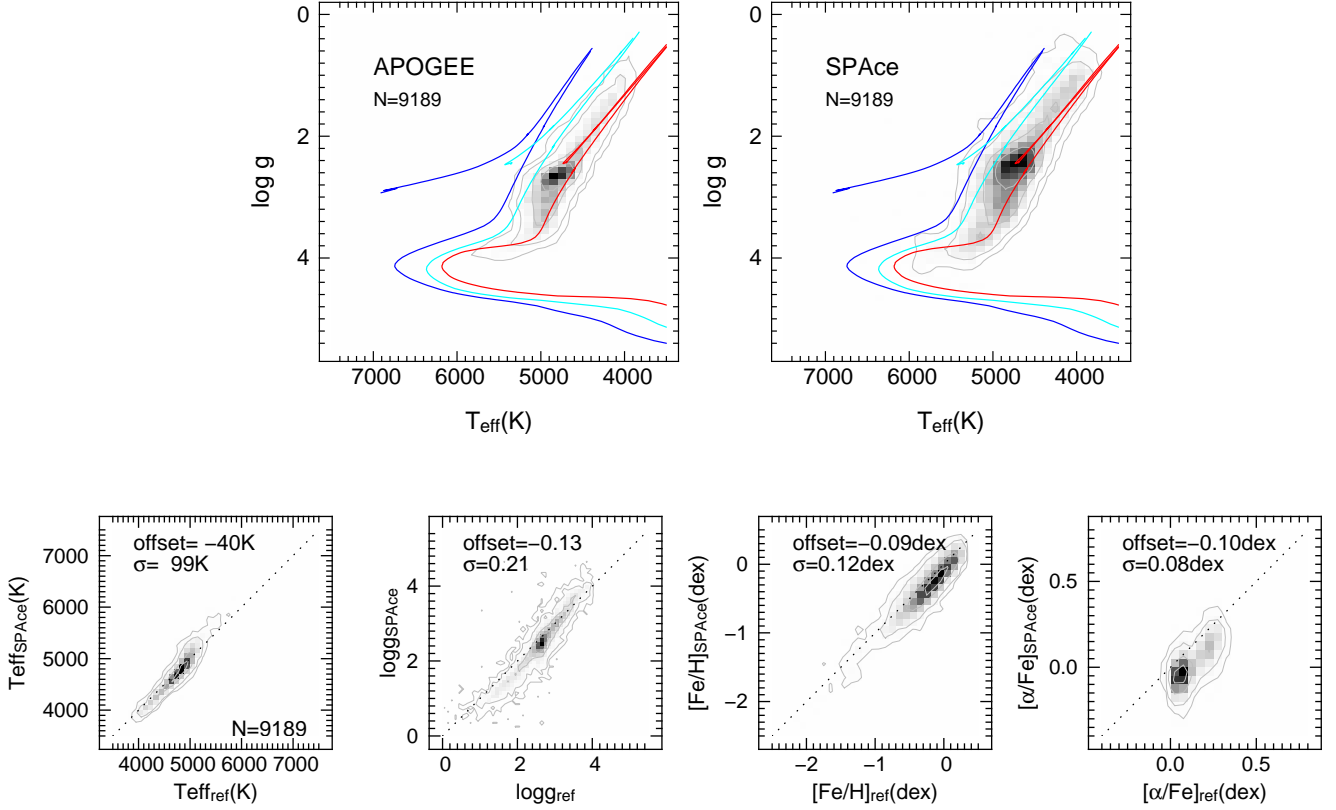


**Figure 4.** An analysis of APOGEE stars with spectra also observed by LAMOST. **Top:** Distributions of the stars with ASPCAP calibrated stellar parameters from the APOGEE spectra (top left panel) and SP\_Ace stellar parameters (top right panel) obtained from the LAMOST spectra with  $S/N_{\text{SP\_Ace}} > 40$ . The red, light blue, and blue lines represent isochrones for  $[M/H] = 0.0$  dex (of 5Gyr age),  $-1.0$  dex and  $-2.0$  dex (10Gyr age), respectively. **Bottom:** comparison of the same SP\_Ace stellar parameters from the LAMOST spectra to the reference ASPCAP parameters from the APOGEE spectra. The reference iron abundance is  $[\text{Fe}/\text{H}]$  (not  $[M/H]$ ) from ASPCAP. The contours enclose 34, 68, 95, and 99% of the sample. A complete version of this plot is given in Fig. 17 of the appendix.

and SP\_Ace parameters. When making this comparison we should first point out that prior tests of the SP\_Ace pipeline have shown a tendency to slightly underestimate  $[\text{Fe}/\text{H}]$ , at a level of around  $-0.05$  dex (see Fig. 17 and accompanying discussion in Boeche & Grebel 2016). We find that SP\_Ace  $[\text{Fe}/\text{H}]$  and  $[\alpha/\text{Fe}]$  abundances appear to be underestimated with respect to APOGEE’s. However, for both parameters the offset appears to be independent of  $[\text{Fe}/\text{H}]$  or  $[\alpha/\text{Fe}]$ , which means that it is straight-forward to shift the SP\_Ace abundances onto the APOGEE scale. A closer look (Fig. 17) shows that the underestimation in  $[\alpha/\text{Fe}]$  has a very weak correlation with the other parameters.  $[\text{Fe}/\text{H}]$ , on the other hand, does show stronger correlations (most notably with gravity and temperature), but the offset appears to be independent of  $[\text{Fe}/\text{H}]$  itself.

Note that in the above discussion we have used the ASPCAP iron abundance  $[\text{Fe}/\text{H}]$ , not the total metallicity  $[M/H]$  (PARAM\_M\_H). The latter quantity has been calibrated onto an  $[\text{Fe}/\text{H}]$ -scale using literature abundances for star clusters, but the former has not (see section 5.4.3 of Holtzman et al. 2015). The lack of an external calibration may influence our findings and so we check the comparison between SP\_Ace and ASPCAP  $[M/H]$  in Fig. 5. For completeness we also include  $[\text{Fe}/\text{H}]$  and  $[\alpha/\text{Fe}]$  from the BACCHUS pipeline (Hawkins et al. 2016), which provides a complementary abundance analysis using APOGEE stars with asteroseismic gravities from Kepler. For the BACCHUS  $[\alpha/\text{Fe}]$  we take the average of

the Mg, Si, Ca and Ti abundances. We can see that when using the ASPCAP  $[M/H]$  there exists a noticeable correlation, which may be due to uncertainties in the external calibration of  $[M/H]$  at the metal-poor end. The correlation disappears (but an offset remains) when comparing SP\_Ace to both ASPCAP  $[\text{Fe}/\text{H}]$  and BACCHUS  $[\text{Fe}/\text{H}]$ . The only differences between BACCHUS and ASPCAP  $[\text{Fe}/\text{H}]$  is a marginal reduction in both the scatter and offset in the former. For  $[\alpha/\text{Fe}]$  the results are also similar between BACCHUS and ASPCAP, although SP\_Ace appears to exhibit a very slight correlation in  $[\alpha/\text{Fe}]$  compared to BACCHUS.

We include three further plots in Appendix B. Fig. 18 shows the  $(T_{\text{eff}}, \log g)$  distributions for stars measured by ASPCAP, BACCHUS, and SP\_Ace, divided into bins of  $[\text{Fe}/\text{H}]$ . For each bin we have over plotted isochrones for the corresponding metallicity. The placement of the SP\_Ace red clump is slightly more consistent with the corresponding isochrones, compared to both APOGEE/ASPCAP and BACCHUS. Furthermore, at lower metallicities ( $[\text{Fe}/\text{H}] \lesssim -0.4$ ) the SP\_Ace red giant branch appears to match the isochrones better than ASPCAP.

The  $[\alpha/\text{Fe}]$  performance is characterized in Figs. 19 and 20 of Appendix B. The former shows the distribution of stars in the  $([\text{Fe}/\text{H}], [\alpha/\text{Fe}])$  plane for SP\_Ace and ASPCAP, while the latter shows a one-to-one comparison for bins of  $[\text{Fe}/\text{H}]$ . The low- and high-alpha sequences are correctly estimated by SP\_Ace, in that SP\_Ace detects

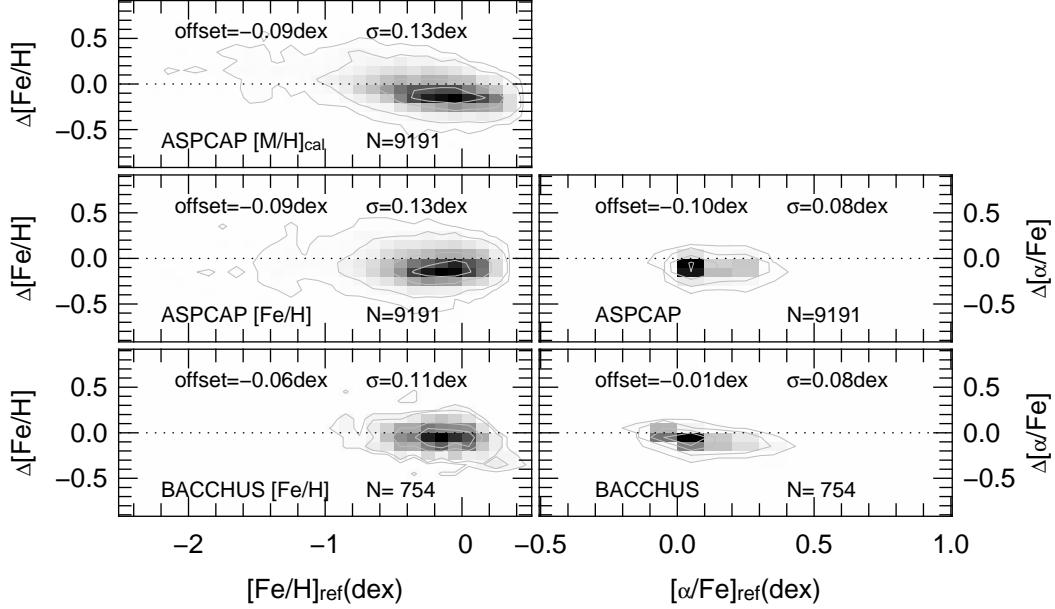


**Figure 5.** Residuals between SP\_Ace and a selection of different reference abundances available for the APOGEE data (SP\_Ace minus reference value) for stars with  $S/N_{\text{SP\_Ace}} > 40$ . The top panel shows the ASPCAP [M/H], the middle panel the ASPCAP [Fe/H] and  $[\alpha/\text{Fe}]$ , all of which are described in Holtzman et al. (2015). The lower panel shows [Fe/H] and  $[\alpha/\text{Fe}]$  from the BACCHUS pipeline (Hawkins et al. 2016). The horizontal axes denote the reference abundance for that particular panel. The contours enclose 34, 68, 95, and 99% of the sample.

a clear shift in alpha between stars from the low- and high-alpha sequences (Fig. 20). Although the LAMOST alphas are not as precise as those from APOGEE (e.g. there is no visible gap between the two sequences), the performance of SP\_Ace is impressive considering the fact that the LAMOST data have a 10 times lower resolution.

#### 4.2. Comparison with Kepler stars

Huber et al. (2014) report the properties of  $\sim 20,000$  stars observed by the the NASA Kepler mission. While the stellar parameters of most of these stars come from a collection of different catalogs with different observational techniques (photometry, spectroscopy),  $\sim 15,500$  of these stars have known oscillations that permit a precise measurement of their surface gravity through asteroseismology. These stars can therefore be used as reference in  $\log g$  for comparison purposes. Our LAMOST sample has 6684 stars in common with Huber et al. (2014). Most of these are giant stars, with a small number of sub-giant and turn-off stars. In Fig. 6 we show the distribution of these stars in the  $(T_{\text{eff}}, \log g)$  plane along with a direct comparison of the parameters, while in Fig. 21 of the Appendix we show the correlations between stellar parameters and the residuals with respect to the reference. In these figures we see an apparent offset in  $T_{\text{eff}}$  and a poor match in [Fe/H] between SP\_Ace and the reference values. The temperature offset appears to be in agreement with the one found by Huber et al. (2014; top panel of Fig. 7), namely a systematic overestimation in their  $T_{\text{eff}}$  value due to the limitations of the Kepler Input Catalogue (KIC) from which they were obtained. Similarly the metallicity offsets are not important, since the Huber et al. (2014) metallicities, which are mainly derived from the KIC, are known to have been underestimated (e.g., Dong et al. 2014). Furthermore the KIC metallicities show an unnatural discrete distribution, which demonstrates their lack of precision. We do know that Huber’s

$\log g$  values are extremely accurate (typically 0.03 dex), and the central bottom panel of Fig. 6 (or the middle row of panels in Fig. 21 of the Appendix) shows a very good match with the SP\_Ace gravity, albeit with an overestimation of  $\sim 0.2$  when  $\log g \lesssim 2$  dex.

Stello et al. (2013) carried out a further analysis of this Kepler sample to distinguish red clump (RC) and red giant branch (RGB) stars following a method similar to Bedding et al. (2011). The analysis by Stello et al. (2013) included only two years of Kepler data. To refine those results we repeated their analysis on 3.5 years of Kepler data. The comparison with these updated seismic results is presented in Fig 7. In the left panels we notice that SP\_Ace correctly positions both the RC and RGB locus on the high metallicity isochrone. The right panels show that SP\_Ace is able to recover accurate gravities for both the RC and RGB samples, although the latter have a slight systematic offset ( $\sim -0.08$  dex). It should be stressed that these results are obtained directly from SP\_Ace without any need for calibrations.

#### 4.3. Main-sequence stars: Comparison with the Geneva-Copenhagen and Gaia-ESO surveys

As the previous sections focused mainly on giant stars, we now utilize two surveys that contain large numbers of main-sequence stars. Our first data set is from the Geneva-Copenhagen Survey (GCS, Nordström et al. 2004), which consists of 16,682 FGK dwarf stars in the immediate solar neighborhood. As reference parameters we adopt those of Casagrande et al. (2011). In this work they derived  $T_{\text{eff}}$  and  $\log g$  from photometry using an infrared flux method (IRFM), where the latter quantity also incorporated the Hipparcos parallax, and derived metallicity from Strömgren photometry. Although we cannot expect high precision from this approach, their parameters are still of great help in determining the robustness of our parameters for dwarf stars. We have



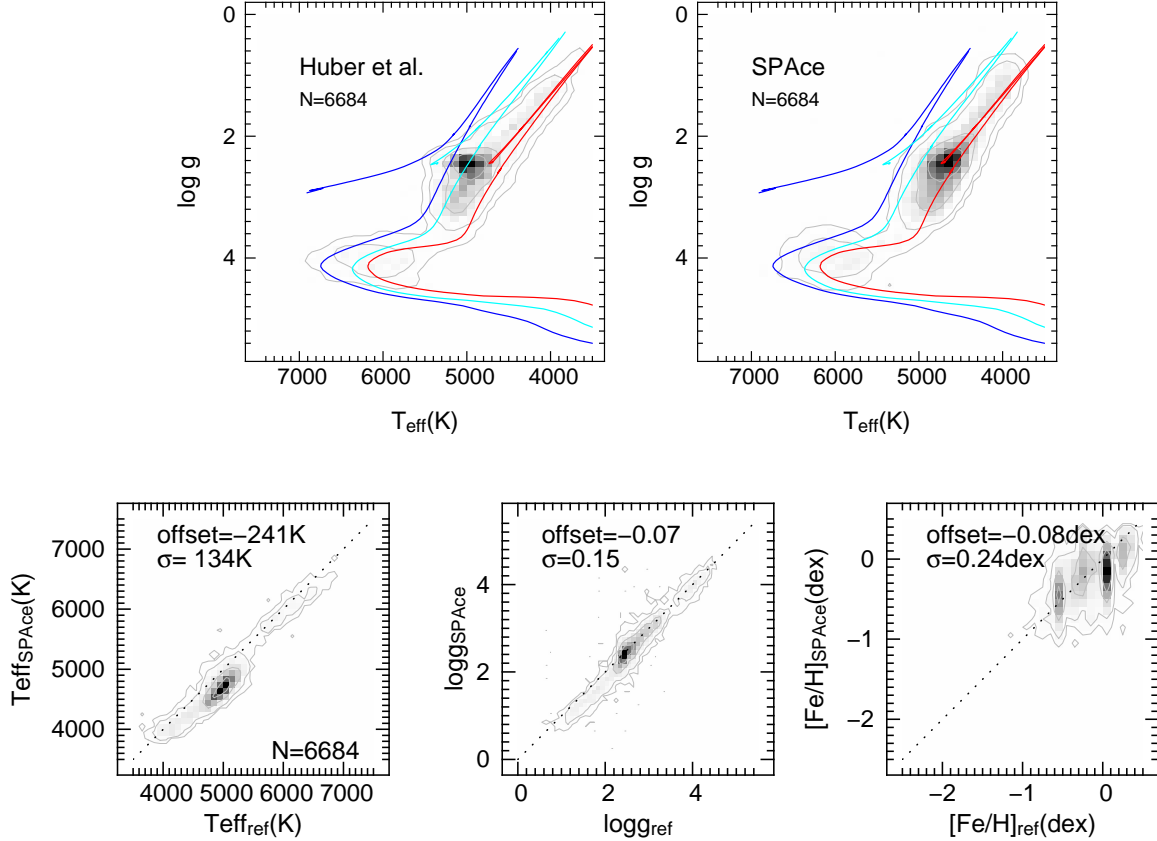


**Figure 6.** **Top:** distributions in the  $(T_{\text{eff}}, \log g)$  plane of the Kepler stars as given by Huber et al. (left panel) and SP\_Ace (right panel), where we have restricted ourselves to stars with  $S/N_{\text{SPAce}} > 40$ . The red, light blue, and blue lines represent the same isochrones as in Fig. 4. **Bottom:** comparison of the SP\_Ace stellar parameters to the reference Huber et al. parameters. The contours enclose 34, 68, 95, and 99% of the sample. A complete version of this plot is given in Fig. 21 of the appendix.

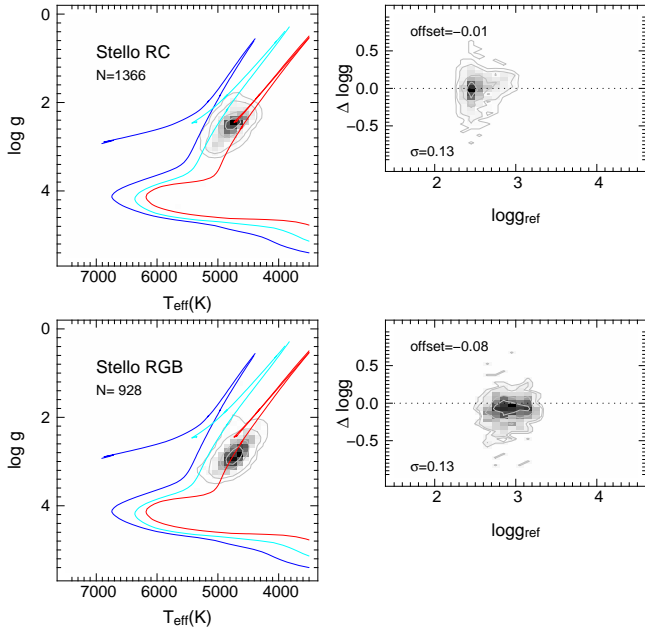


**Figure 7.** Top panels: comparison of SP\_Ace to seismic gravities from the updated Stello et al. (2013) sample (see Section 4.2) for 1366 red clump stars for stars with  $S/N_{\text{SPAce}} > 40$ . The left panel shows the distribution of SP\_Ace parameters in the  $(T_{\text{eff}}, \log g)$  plane, while the right panel shows the  $\log g$  residuals between SP\_Ace and Stello. Bottom panels: As above, but for 928 red giant stars.

413 stars in common with GCS, out of which 233 have  $S/N_{\text{SPAce}} > 40$  and SP\_Ace stellar parameters. Their distributions in the  $(T_{\text{eff}}, \log g)$  plane and a direct comparison are shown in Fig. 8, while the full correlations between the parameters are in Fig. 22 of the Appendix.

Our second data set is from the Gaia-ESO survey (GES, Gilmore et al. 2012), which provides precise stellar parameters from high resolution spectra obtained with the ESO UVES and Giraffe spectrographs (with a spectral resolution of  $\sim 60\,000$  and  $\sim 20\,000$ , respectively). Using GES DR3 we have found 390 stars in common with LAMOST that have non-null GES parameters  $T_{\text{eff}}$ ,  $\log g$ , and  $[\text{Fe}/\text{H}]$ . Out of these, 146 have  $S/N_{\text{SPAce}} > 40$  and SP\_Ace stellar parameters. Comparisons between SP\_Ace and GES are presented in Fig. 9 and in Fig. 23 of the Appendix.

For both the GCS and GES comparisons we can see that  $T_{\text{eff}}$  and  $\log g$  match the reference parameters fairly well, with small offsets. However, for the GCS the iron abundance exhibits a negative offset (i.e. SP\_Ace is underestimating  $[\text{Fe}/\text{H}]$  compared to GCS), especially for the hotter, lower-gravity dwarfs (see upper-left and upper-middle panels of Fig. 22). A handful of these stars also have significantly under-estimated gravities compared to the GCS value. There is weak evidence for a similar metallicity trend in the GES comparison (Fig. 23), although the paucity of stars in this region of parameter space (i.e.,  $T_{\text{eff}} \gtrsim 6000$  K and  $3 \lesssim \log g \lesssim 4$  dex) makes it hard to draw any firm conclusions.

From Fig. 23 we can see that there is an underestimation in  $[\alpha/\text{Fe}]$  of  $\sim 0.1$  dex when comparing SP\_Ace to GES, which is similar to the one seen when comparing SP\_Ace to APOGEE (Section 4.1).

#### 4.4. Uncertainties

SP\_Ace estimates  $1\sigma$  uncertainties along with the stellar parameters for each star. It does this by considering the shape of the  $\chi^2$  hyper-surface and identifying the upper and lower parameter limits for which  $\chi^2 = \chi^2_{\min} + \Delta\chi^2$ , where  $\Delta\chi^2$  depends on the number of degrees of freedom (for details see section 7.6 in Boeche & Grebel, 2016). For a correct validation of these uncertainties we would need to compare the SP\_Ace results to reference parameters having no (or very small) errors, which would allow us to infer the precision from the standard deviation of the discrepancies and the accuracy from the systematic offsets. Unfortunately this is not possible because the reference parameters are also affected by stochastic and systematic errors. However, we can overcome this by adding in quadrature the errors from both SP\_Ace and the reference data set, although of course this relies on the assumption that the reference errors are accurately reported.

The comparison between the distribution of the discrepancies (SP\_Ace minus reference parameter) and the SP\_Ace errors for giant stars is reported in the three top left panels of Fig. 24. As expected, the discrepancies become larger as the  $S/N_{\text{SPAce}}$  decreases. The red dots show the expected magnitude of the standard deviation, as estimated by adding in quadrature both the SP\_Ace and ASPCAP uncertainties. For most of these parameters the SP\_Ace errors look like they are providing a fair approximation to the observed scatter, with the red dots agreeing with the  $1\sigma$  limit of the distribution of discrepancies (indicated with black error bars). For  $T_{\text{eff}}$  and  $[\alpha/\text{Fe}]$  SP\_Ace appears to be overestimating the uncertainties slightly, especially for  $[\alpha/\text{Fe}]$  in the low- $S/N$  regime. On the other hand, it appears to underestimate the errors for  $[\text{Fe}/\text{H}]$ . The magnitude of this underestimation is hard to quantify because the reported errors on the ASPCAP  $[\text{Fe}/\text{H}]$  are exceedingly small (0.03 dex) and so it is unclear which method is underestimating the size of their errors. As an example, if we consider moderately low  $S/N_{\text{SPAce}}$  stars (around  $40 \lesssim S/N_{\text{SPAce}} \lesssim 70$ ), we find that in order to bring our estimated errors into agreement with the standard deviation of the discrepancy, we would need to inflate both SP\_Ace and ASPCAP errors by around 30%. Repeating this exercise for  $[\alpha/\text{Fe}]$  indicates that for the same stars we would need to reduce the SP\_Ace errors by around 40% in order to match the observed standard deviation.

In the top right panel of Fig. 24 we compare the SP\_Ace  $\log g$  to the Huber et al. values. Because of the high precision of the seismic gravities (with typical uncertainties of 0.03 dex), we expect that the scatter reflects the magnitude of the SP\_Ace errors. Apart from a slight overestimation at the low- $S/N_{\text{SPAce}}$  end, the  $\log g$  errors provide a good match to the observed scatter. However, if we look at the mean of the discrepancy (given by the black dots) there appears to be a slight correlation with  $S/N_{\text{SPAce}}$ ; as well as the previously identified offset (see Section 4.2), the SP\_Ace  $\log g$  appears to suffer from a larger underestimation for lower  $S/N_{\text{SPAce}}$  spectra. At

higher  $S/N_{\text{SPAce}}$  ( $\sim 100$ ) the offset is barely noticeable, amounting to less than 0.05 dex, but this increases to as much as 0.15 dex at lower  $S/N_{\text{SPAce}}$  ( $\sim 30$ ). The same analysis is presented on the bottom panels of Fig. 24 for the Gaia-ESO survey stars. This sample is more representative of dwarf stars, since it contains only a small fraction of giants. Although there are also far fewer stars to compare to, and hence the distributions (especially  $T_{\text{eff}}$ ) are a little harder to interpret, the trends we saw for giants are replicated. Namely our errors appear to be reliable for  $T_{\text{eff}}$  and  $\log g$ , but are slightly over- and under-estimated for  $[\text{Fe}/\text{H}]$  and  $[\alpha/\text{Fe}]$ , respectively. The correlation between SP\_Ace  $\log g$  and  $S/N_{\text{SPAce}}$  that was found for the Huber sample appears to persist for the GES, implying that this is common for dwarf stars as well.

## 5. THE CATALOG

Out of the 2 052 662 processed spectra, SP\_Ace derived parameters for 1 097 231 spectra. For half of the spectra SP\_Ace did not output any results since it failed to converge for one or more parameters. The main reason for the failure of convergence is the low  $S/N$ : for spectra with  $\text{SNRI} < 20$  (736 929),  $\sim 80\%$  failed to converge, while for spectra with  $\text{SNRI} > 20$  (1 315 733),  $\sim 27\%$  failed to converge. As we will show later (Section 5.2), this problem is not unique to SP\_Ace; in fact, the fraction low- $S/N$  spectra that can be processed by SP\_Ace is similar to that of the official LAMOST pipeline (LASP). Other reasons for failure can be: stars with stellar parameters out of the limits of the GCOG library (e.g., too hot or too cool); too high a RV; spectra of non-stellar, or peculiar objects.

The final results are sorted and described as in Table 1. In this table we include the parameter  $[\text{M}/\text{H}]$ , which has not previously been mentioned. This parameter represents the metallicity of the atmosphere model that was used to compute the GCOGs, which were in turn used to derive the spectrum's parameters. These atmosphere models were taken from ATLAS12 by Castelli and Kurucz, (2003) and have  $[\alpha/\text{Fe}] = 0$ . This means that their nominal metallicity is equal to the iron abundance. Since iron is the main driver of the metallicity, one finds that in our catalog the metallicity  $[\text{M}/\text{H}]$  is usually very close (or equal) to  $[\text{Fe}/\text{H}]$ . To obtain a more general metallicity index that also includes the contribution of the  $\alpha$  elements, we suggest using the following formula

$$[\text{M}/\text{H}]^{\text{chem}} = [\text{Fe}/\text{H}] + \log(0.638 \cdot 10^{[\alpha/\text{Fe}]} + 0.362), \quad (5)$$

given by Salaris et al. (1993).

We remember that our  $[\text{Fe}/\text{H}]$  parameter represents the abundance of all non- $\alpha$ -elements as if they were a single element, to which iron is the major contributor. The total number of absorption lines measured to derive the abundance of the  $[\text{Fe}/\text{H}]$  parameter is reported by the  $N_{\text{lin}}$  parameter. Consequently, the abundances will be more robust for spectra with higher values of  $N_{\text{lin}}$ . The same applies to the  $[\alpha/\text{Fe}]$  parameter, which represents the abundance of the  $\alpha$ -elements Mg, Si, Ca, and Ti derived as if they were one single element.

In Figs. 10 and 11 we show the distributions of  $\log g$  vs  $T_{\text{eff}}$  and  $[\alpha/\text{Fe}]$  vs  $[\text{Fe}/\text{H}]$  for our SP\_Ace catalog, divided into high and low  $S/N_{\text{SPAce}}$ . We here employ

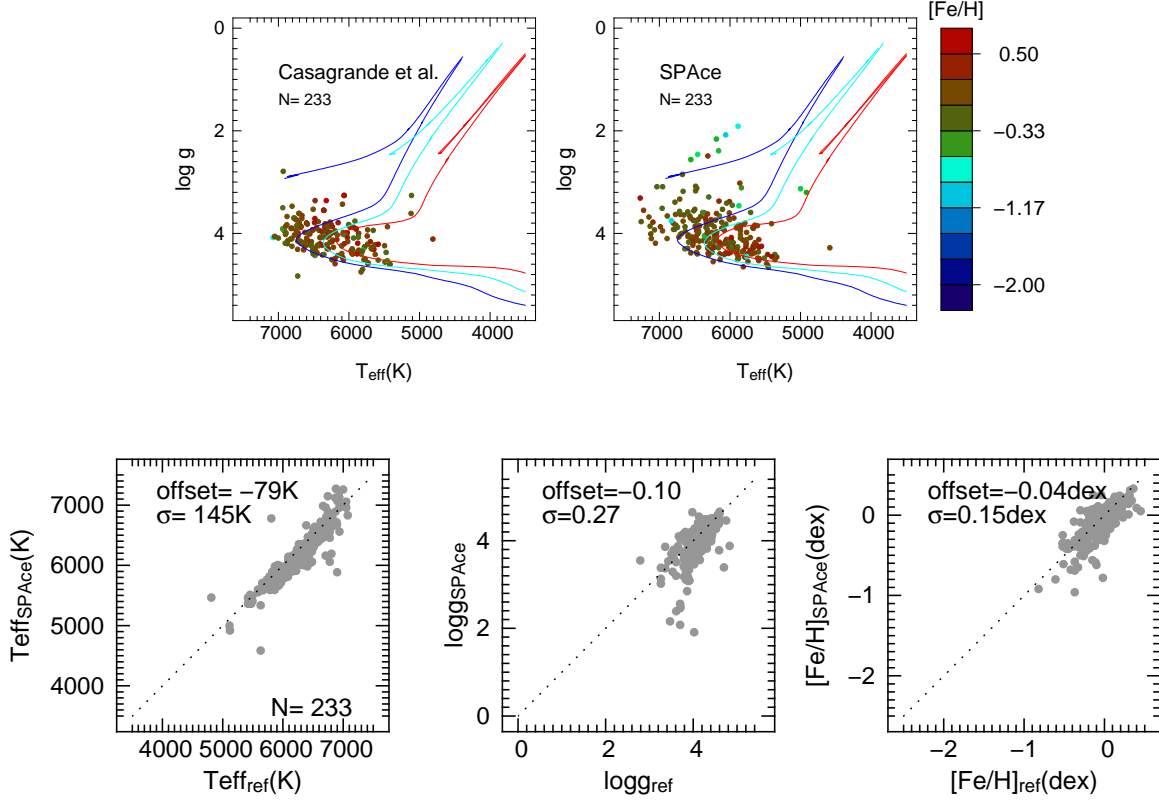


**Figure 8.** **Top:** distributions in the  $(T_{\text{eff}}, \log g)$  plane of the GCS stars as given by Casagrande et al. stars (left panel) and SP\_Ace (right panel) for stars with  $S/N_{\text{SP\_Ace}} > 40$ . The red, light blue, and blue lines represent the same isochrones as in Fig. 4. **Bottom:** comparison of the SP\_Ace stellar parameters to the reference Casagrande et al. parameters. A complete version of this plot is given in Fig. 22 of the appendix.

$S/N_{\text{SP\_Ace}} = 40$  as a discriminator between the stellar parameters with “fair” and “good” accuracy and, as expected, the dispersion of the data observed in these figures reflects this. In Fig. 10 the red dotted line delineates a sample of cool dwarf stars that, as they are placed far from the expected isochrones, are most likely subject to a systematic error in gravity. This is discussed in the following section.

### 5.1. Known systematic errors

In Section 4 we demonstrated the successful performance of SP\_Ace and found that there is good agreement with reference data sets. We also pointed out the presence of some systematic errors. The comparison with the Kepler stars showed that SP\_Ace underestimates the gravity ( $\sim -0.2$ ) for giants with  $\log g \lesssim 2$ , while the comparison with the GCS and GES stars revealed an underestimation of the iron abundance for stars with  $T_{\text{eff}} \gtrsim 6000 \text{ K}$  and  $3 \lesssim \log g \lesssim 4$  (see also later in this section). Still, we did not test the performance for cool dwarf stars because of a lack of reference stars in this  $T_{\text{eff}}\text{-}\log g$  region. As was shown in Fig. 10, it appears that SP\_Ace underestimates gravity for the cool dwarfs. These have been delineated by the red dotted line in this figure. The cause is unclear, but may be due to one or more of the following reasons: the physics of the adopted 1D atmosphere models is deficient, i.e., does not match the real conditions; the assumption of LTE is invalid; and/or the presence of molecular lines (which are neglected by SP\_Ace) are affecting the atmospheres of cool dwarfs. Although this manifests itself in an underesti-

mation in gravity, the problem could propagate into the other parameter estimates as well. Therefore we recommend that the parameters for these cool dwarfs are not to be trusted. Since we have no way to determine precisely where this systematic becomes significant, the red dotted boundary in Fig. 10 was determined by eye. These are the stars for which  $T_{\text{eff}} < 4800 \text{ K}$  and  $\log g > 0.0015 \cdot T_{\text{eff}} - 3.25$  and they are flagged with  $\text{FLAG} = 0$  in the catalog. They represent 3% of the total sample.

Additional potential systematic errors are shown in Fig. 12. The left and middle panels appear to show a dependence on the mean  $[\text{Fe}/\text{H}]$  with  $S/N_{\text{SP\_Ace}}$ , which has an amplitude of  $\sim 0.1 \text{ dex}$ , for both dwarfs (left) and giants (middle). Although this may be due to some feature of the survey selection function (e.g., the distribution of latitude or distance), we have been unable to pinpoint a cause and therefore conclude that this is likely to be a systematic inherent to SP\_Ace. The right panel of Fig. 12 shows our final potential systematic, which has already been discussed above in Section 4.3. In that section we pointed out that hot ( $T_{\text{eff}} \gtrsim 6000 \text{ K}$ ) dwarfs appear to have underestimated  $[\text{Fe}/\text{H}]$ . The same problem appears to manifest itself in the right panel of Fig. 12, where there is a clear deficiency of hot, iron-abundant stars, i.e., for these stars the iron abundance is being underestimated. Note that the  $T_{\text{eff}}$  upper limit for SP\_Ace is 7400 K, which means that for any spectrum of a higher temperature star SP\_Ace is expected to exit with no result. Moreover, we must remember that the SP\_Ace line list was built using 5 standard stars, the hottest of which is Procyon with

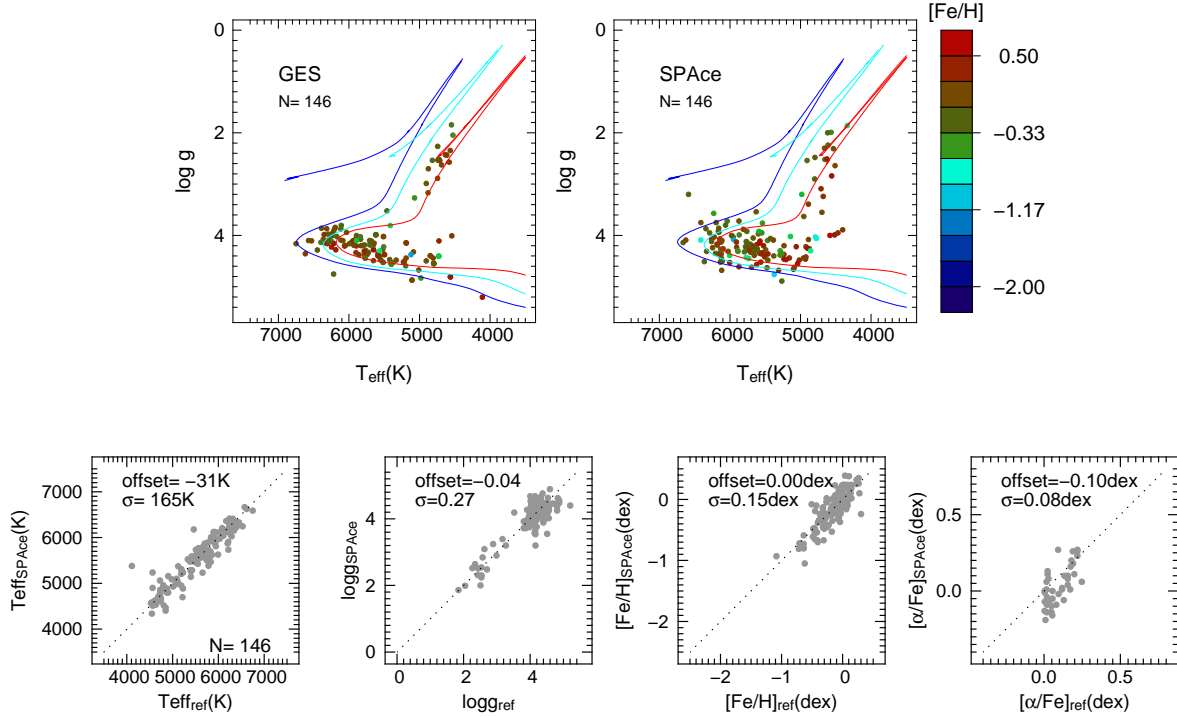


**Figure 9.** **Top:** distributions in the  $(T_{\text{eff}}, \log g)$  plane of the stars as given by the GES stars (left panel) and SP\_Ace (right panel) for stars with  $S/N_{\text{SP\_Ace}} > 40$ . The red, light blue, and blue lines represent the same isochrones as in Fig. 4. **Bottom:** comparison of the SP\_Ace stellar parameters to the reference GES parameters. A complete version of this plot is given in Fig. 23 of the appendix.

$T_{\text{eff}}=6554$  K. As a consequence for  $T_{\text{eff}}$  higher than that of Procyon the stellar spectra may contain absorption lines that are not included in the line list, which could potentially lead to systematic errors.

For the sake of completeness, we also mention a  $S/N$  dependent bias against low metallicity stars. The lower the metallicity of a star, the weaker are its absorption lines. This means that for a star of lower metallicity, the  $S/N$  must be higher in order to make the lines identifiable through the noise. If too many lines are not identifiable, the analysis can fail, leading to an underestimation of the number of low metallicity stars. To explain the bias better, in the following we propose a different point of view of this problem.

We usually refer to the  $S/N$  as the ratio between the continuum level and the noise level. However, in measuring the strength<sup>9</sup> of an absorption line, we should consider the ratio between the line strength and the noise level, a ratio that we may call “line strength-to-noise” ratio ( $L/N$ ). For a fixed level of noise, the  $L/N$  diminishes with the line strengths. Therefore, for small  $L/N$  the measured strength of the line is more uncertain. If  $L/N < 3$  we can no longer firmly detect the line. SP\_Ace selects the lines (to be used to build the spectrum model) as a function of their detectability: if a line (or a collection of blended lines) has an expected maximum strength much smaller than the noise, then it is neglected. It follows that the noise level sets a lower limit to the strength of the detectable absorption lines and those which lie under this limit are not considered anymore. Because the

strengths of the lines diminish with the metallicity of the stars, the number of the absorption lines considered diminishes with the metallicity of the star. Eventually, the number of measurable lines becomes too small to derive the stellar parameters and the analysis fails. This causes a bias against low metallicity stars, and this bias is greater for lower  $S/N$  spectra. The same bias has a greater effect on hot dwarfs, as opposed to cold giants, because the absorption lines of the former have lower EWs (for a given metallicity). Computing a reliable correction for this bias would require complex modeling and hence we do not tackle the problem here.

## 5.2. Comparison between SP\_Ace and LASP

We now compare the performance of SP\_Ace and the official LAMOST pipeline LASP<sup>10</sup> (Luo et al. 2015), using two different methods applied to the same spectra. The first issue to consider is the total number of converged spectra. In this aspect the performance of the two pipelines is similar. The total number of converged spectra is 1125722 for LASP and 1097010 for SP\_Ace. The ability of each pipeline to process low- $S/N$  spectra is also similar; if we consider the 506658 stars with LAMOST SNRI of between 20 and 40, we find that LASP converges for 297597 while SP\_Ace converges for 301939. Note that not all of these spectra will have unusable parameters; of these 301939 stars, 70% have  $S/N_{\text{SP\_Ace}} > 30$  and 38% have  $S/N_{\text{SP\_Ace}} > 40$ . On the top of Fig. 13 we compare the LASP and SP\_Ace distributions in the  $(T_{\text{eff}}, \log g)$  plane for all DR1 spectra that have  $S/N_{\text{SP\_Ace}} > 40$  and parameters estimated by both codes. There are some differences, such as i) for cool dwarf

<sup>9</sup> Here the term “strength” refers to the intensity of the absorption line. This can be also taken to mean as the ratio between the depth of the line over the continuum level and a proxy of the EW.

<sup>10</sup> Here we adopt the parameters derived using the DR3 version of LASP.



**Table 1**  
Description of the catalog

Field	Name	Format	Unit	Description
1	OBSID	integer	...	unique identification number of the spectrum
2	designation	string	...	object designation
3	ra	float	deg	object Right Ascension
4	dec	float	deg	object Declination
5	obsdate	...	...	date of observation
6	lmjd	integer	...	local modified Julian date
7	planid	string	...	plan ID in use
8	spid	integer	...	spectrograph ID
9	fiberid	integer	...	fiber ID of object
10	RVb	float	km s <sup>-1</sup>	radial velocity correction of the blue part of the spectrum
11	RVr	float	km s <sup>-1</sup>	radial velocity correction of the red part of the spectrum
12	FWHMb	float	Å	Full-Width-Half-Maximum of the blue part of the spectrum
13	FWHM <sub>r</sub>	float	Å	Full-Width-Half-Maximum of the red part of the spectrum
14	S/N	float	...	signal-to-noise as computed by SP_Ace
15	$T_{\text{eff}}$	float	K	effective temperature
16	inf	float	K	effective temperature lower limit
17	sup	float	K	effective temperature upper limit
18	log $g$	float	dex	gravity
19	inf	float	dex	gravity lower limit
20	sup	float	dex	gravity upper limit
21	[M/H]	float	dex	nominal metallicity of the atmosphere model
22	inf	float	dex	nominal metallicity lower limit
23	sup	float	dex	nominal metallicity upper limit
24	[Fe/H]	float	dex	iron abundance
25	inf	float	dex	iron abundance lower limit
26	sup	float	dex	iron abundance upper limit
27	Nlin	integer	...	number of absorption lines used to derive the iron abundance
28	[ $\alpha$ /H]	float	dex	$\alpha$ -element abundance
29	inf	float	dex	[ $\alpha$ /H] lower limit
30	sup	float	dex	[ $\alpha$ /H] upper limit
31	Nlin	integer	...	number of absorption lines used to derive [ $\alpha$ /H]
32	flag	integer	...	spectra with FLAG=0 must be rejected or treated with extreme caution (Section 5.1)
33	class	string	...	LAMOST classification of the object (Section 3.3)
34	z	float	...	red shift of object (from the LAMOST pipeline)
35	z_err	float	...	red shift error (from the LAMOST pipeline)

stars SP\_Ace derives log  $g$  values that are systematically too low (this is clearly detectable by eye at  $T_{\text{eff}} < 4800\text{K}$ , but it extends, at a lesser degree, to higher  $T_{\text{eff}}$ ), ii) for  $T_{\text{eff}} \gtrsim 5600\text{ K}$  the LASP gravity distribution unnaturally peaks at log  $g \sim 4.2$ , iii) most of the LASP red giant branch stars do not have log  $g$  values lower than  $\sim 2$  while the SP\_Ace gravities extend to lower values. Besides, the parameters from LASP closely follow the isochrones, even for very low S/N where we would expect the errors to be larger (see bottom panels of Fig. 13). This is due to one of the LASP features, i.e., stars are placed on areas of the parameter space where the standard stars (which are employed as templates) lie. If there are no templates for a particular location in parameter space (for instance on the horizontal branch or far from the isochrones), then the LASP pipeline is unable to place a star there. As a consequence the LASP pipeline renders a more good-looking distribution, but it can also create hidden systematic errors for those stars that are not represented in the template sample. For low S/N spectra the LASP parameters lack the natural dispersion expected for such spectra. Fig. 14 shows a detailed comparison of the two approaches. They agree fairly well for  $T_{\text{eff}}$  and log  $g$  although for cool dwarfs we find the systematic errors already discussed in Section 5.1. The good general agreement between the two [Fe/H] values is shown in the same figure, together with the known systematic offsets for both extremes of the temperature range for

dwarf stars (over- and under-estimated for  $T_{\text{eff}} < 5500$  and  $T_{\text{eff}} > 6500\text{ K}$ , respectively).

### 5.3. Comparison between SP\_Ace and The Cannon

Recently Ho et al. (2017b) used *The Cannon* (Ness et al., 2015) to derive stellar parameters and abundances of the alpha-elements and the individual elements C and N of giant stars from the LAMOST DR2 internal data release. *The Cannon* has been trained on a set of spectra of objects that LAMOST has in common with APOGEE. In their work, Ho et al. demonstrated the consistency between their stellar parameters and those obtained by APOGEE from high-resolution spectra. As previously done with the LASP pipeline, we now compare the Ho et al. results with the ones obtained with SP\_Ace. Out of the 454 450 spectra considered by Ho et al., we have in common 219 360 spectra belonging to LAMOST DR1.

The distribution in the ( $T_{\text{eff}}$ , log  $g$ ) plane of the spectra with  $S/N_{\text{SPAce}} > 40$  is shown on the top of Fig. 15. *The Cannon* places RC stars in a similar position to APOGEE (Fig. 4), although the former are located at slightly higher gravity, in a position more suitable for RGB stars. We investigate this further using the asteroseismic log  $g$  values from Huber et al. (2014) for the two samples of RC and RGB stars classified by Stello et al. (which were introduced in Section 4.2, see Fig. 7). From its high-resolution spectroscopy APOGEE finds offsets of 0.14 and -0.03 dex for the RC and RGB, respectively

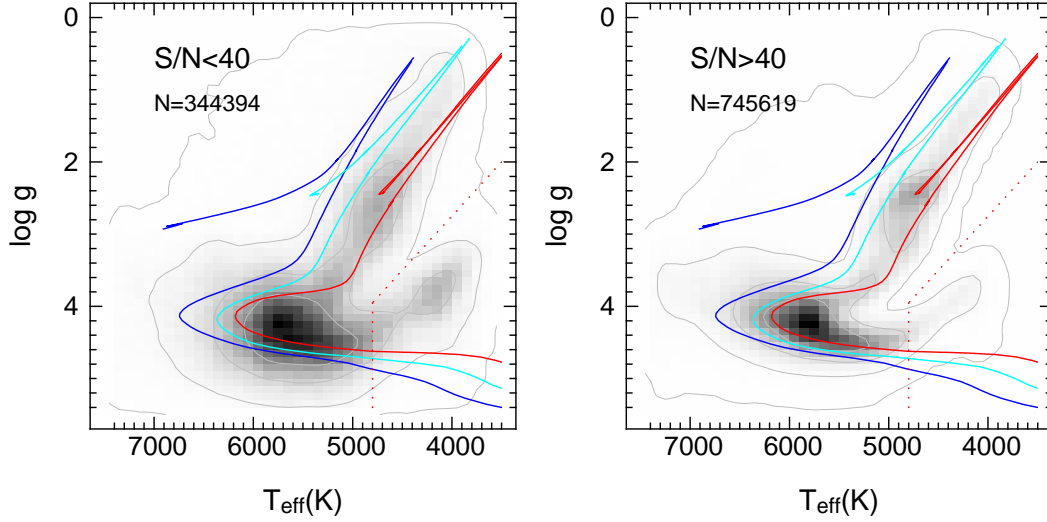


**Figure 10.** Distributions of SP\_Ace parameters ( $T_{\text{eff}}$ ,  $\log g$ ) for the LAMOST DR1 stars with  $S/N_{\text{SPAce}}$  smaller and larger than 40. The red, light blue, and blue solid lines represent the same isochrones as in Fig. 4. The cool dwarfs delineated by the red dotted line appear to be subject to a systematic error in gravity (see Section 5.1). The contours enclose 34, 68, 95, and 99% of the sample.

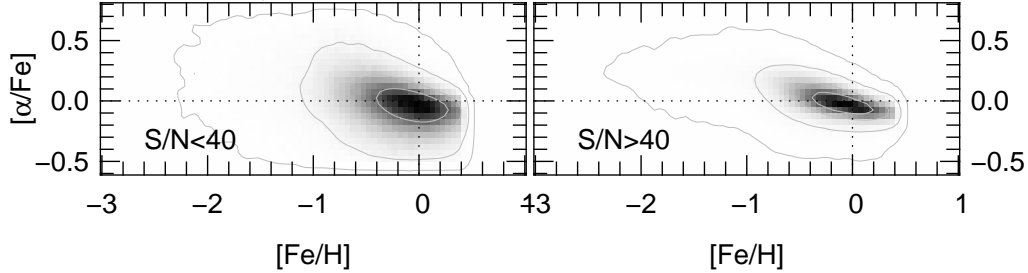


**Figure 11.** Distributions of SP\_Ace abundances ( $[\text{Fe}/\text{H}]$ ,  $[\alpha/\text{Fe}]$ ) for the LAMOST DR1 stars with  $S/N_{\text{SPAce}}$  smaller and larger than 40. The contours enclose 34, 68, 95, and 99% of the sample.

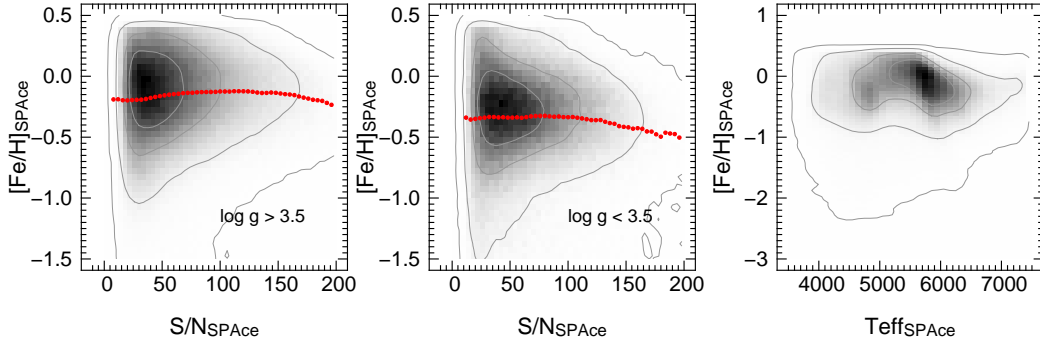


**Figure 12.** Density distributions of  $[\text{Fe}/\text{H}]$  as a function of  $S/N_{\text{SPAce}}$  for dwarf (left panel) and giant stars (middle panel). The red dots trace the average of the  $[\text{Fe}/\text{H}]$  distribution for each  $S/N$  bin. Right panel: density distribution of  $[\text{Fe}/\text{H}]$  as a function of  $T_{\text{eff}}$  for the whole sample. The contours enclose 34, 68, 95, and 99% of the sample.

(from samples of 1045 and 661 stars, respectively). These results are to be expected as APOGEE gravities are calibrated onto the asteroseismic RGB sample of Pinsonneault et al. (2014), hence the good agreement for the RGB and systematic overestimation for the RC (see Fig. 4 of Holtzman et al. 2015). If we now consider the low-resolution LAMOST spectra as analyzed by *The Cannon*, we find that its performance is subject to larger systematic errors with offsets of 0.31 and 0.15 dex, respectively (from samples of 265 and 112 stars, respectively). This can be compared to the performance of SP\_Ace (Fig. 7), which has offsets of only -0.01 and -0.08 dex, respectively (from 1366 and 928 stars, respectively). The scatter for SP\_Ace is marginally larger than for *The Cannon* (0.13 vs

0.10 dex), but the systematic errors are significantly less. The fact that the systematic errors are smaller than even the high-resolution data from APOGEE demonstrates the efficacy of SP\_Ace for recovering accurate gravities from LAMOST spectra. Note that other machine learning methods have had more success at fitting gravities (e.g. Liu et al. 2015), but a comprehensive comparison of all pipelines is beyond the scope of this study.

The correlations between the residuals SP\_Ace minus *The Cannon* and the *The Cannon* parameters, as shown in Fig. 16, are similar to those obtained for the APOGEE data (Fig. 17). This is not surprising since *The Cannon* has been trained with a set of spectra labeled with the APOGEE data. The same systematics are observed in

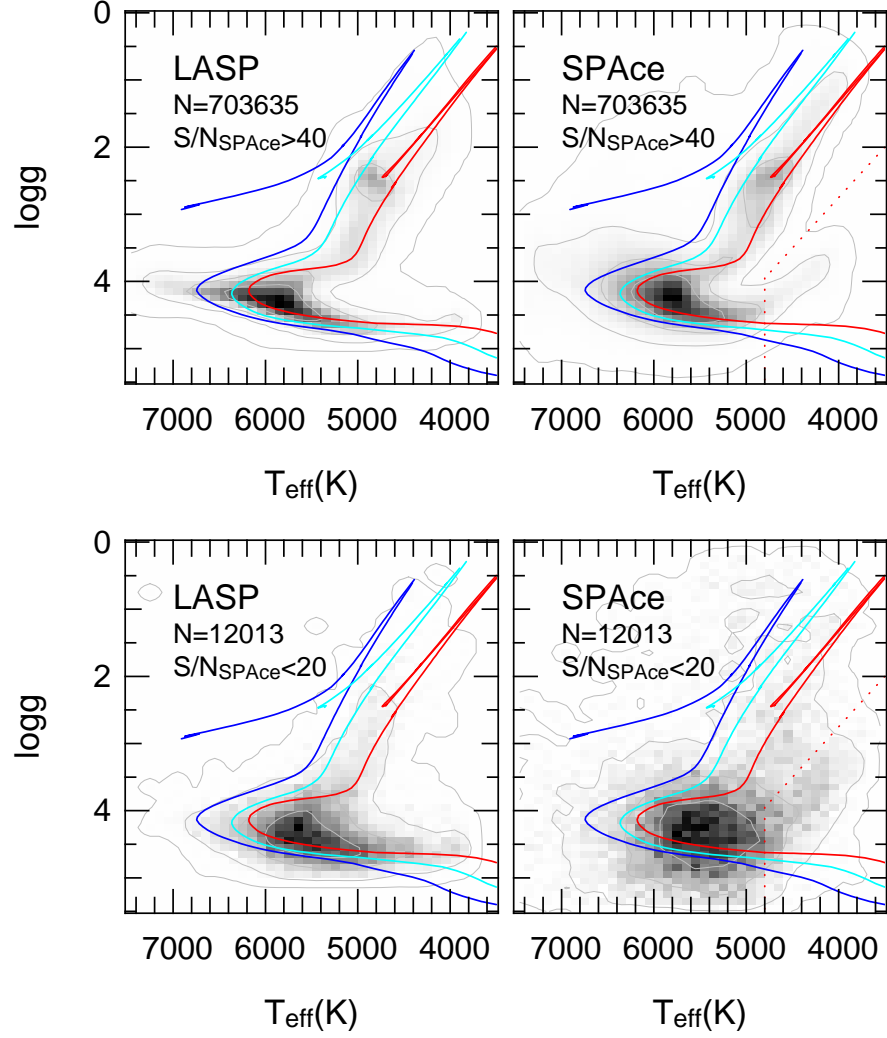


**Figure 13.** Density distribution of the LAMOST spectra in the  $(T_{\text{eff}}, \log g)$  plane for LASP (left panel) and SP\_Ace (right panel) for stars with  $S/N_{\text{SP\_Ace}} > 40$  (top) and  $S/N_{\text{SP\_Ace}} < 20$  (bottom). The red, light blue, and blue lines represent the same isochrones as in Fig. 4. The red dotted line highlights the region where the stars have systematically underestimated gravities. This is discussed in Section 5.1.

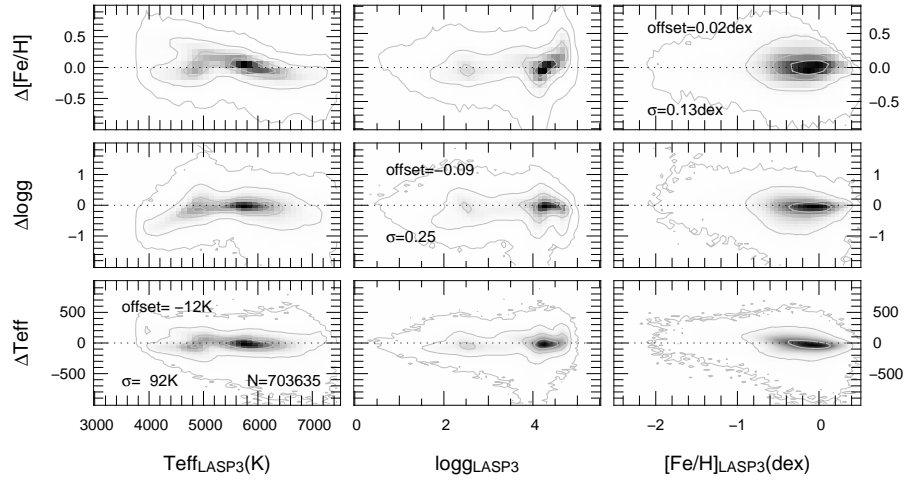


**Figure 14.** Residuals (SP\_Ace minus LASP) of the stellar parameters with respect to the LASP values for stars with  $S/N_{\text{SP\_Ace}} > 40$ .

gravity,  $[\text{Fe}/\text{H}]$ , and  $\log g$ . However, there is a group of stars for which SP\_Ace assigns a higher  $T_{\text{eff}}$  than *The Cannon* (stars at *The Cannon*  $\log g \sim 3.5$ ) and the same stars also have higher SP\_Ace  $\log g$ . *The Cannon* locates these stars on the red giant branch while SP\_Ace classifies them as sub-giants. Unfortunately, in this region of parameter space there are too few stars with asteroseismic gravities to clarify the origin of this offset.

On the bottom of Fig. 15 we report the distributions of low S/N<sub>SP\_Ace</sub> stars in the  $(T_{\text{eff}}, \log g)$  plane for *The Cannon* and SP\_Ace. While at low S/N the SP\_Ace parameters show a scatter around the isochrones (as expected) the lack of dispersion shown by *The Cannon* is similar to the LASP pipeline. We make the same comment as before, namely that codes relying on training sets of spectra that do not uniformly cover the parameter space tend to assign stellar parameters to regions covered by the training sets. This means that they lack the natural scatter due to the uncertainties coming from working at low S/N. This aspect should be further investigated to establish the presence (or lack) of possible systematic errors as a function of the S/N, particularly in regions of parameter space that are not covered by stars in the training set.

## 6. CONCLUSIONS

We have used the code SP\_Ace to derive stellar parameters for 1097231 stellar objects from the LAMOST DR1 catalog. In addition to the parameters  $T_{\text{eff}}$ ,  $\log g$ , and  $[\text{Fe}/\text{H}]$  (which are also given by the LAMOST LASP pipeline) we have also derived the alpha abundance  $[\alpha/\text{H}]$ . By comparing our results to high precision parameters for stars from surveys such as APOGEE, the Gaia-ESO survey, the Geneva-Copenhagen Survey, and the Kepler mission, we have confirmed the ability of SP\_Ace to derive stellar parameters and chemical abundances for FGK stars. This has also allowed us to demonstrate the robustness of our results. We have highlighted the presence of some systematic errors in our results, such as the overestimation of  $\log g$  for cold dwarfs, an underestimation of gravity for  $\log g \lesssim 2$ , and a bias against hot metal rich dwarfs. We have also shown that the SP\_Ace error estimates look reliable when compared to the residuals between our results and these reference parameters.

We compared our results to other pipelines which have been used on LAMOST spectra, namely the LASP and *The Cannon* pipelines. The comparison between the three pipelines can be summarized as follows:

- SP\_Ace shows a systematic error in  $\log g$  for dwarf stars cooler than  $T_{\text{eff}} < 4800$  K while LASP and *The Cannon* perform well in this parameter region.

*Cannon* perform well in this parameter region.

- LASP shows an excess of stars with  $\log g \sim 4$  that is not expected and not seen in the SP\_Ace results.
- The LASP results are biased against giant stars with  $\log g < 2$ , which is unexpected as these stars are detected by SP\_Ace and *The Cannon*.
- The position of the RC stars is in good agreement with the isochrones for LASP and SP\_Ace while it is overestimated in  $\log g$  by *The Cannon* (very likely due to the APOGEE training set used by *The Cannon*, which shows the same systematic).
- At low S/N, SP\_Ace's stellar parameters show the natural dispersion expected from spectra that hold little or no information. The other two pipelines follow the isochrones much more closely, which is a consequence of how they estimate parameters (i.e. both techniques use of training sets whose distribution closely match the isochrones). This artificial lack of dispersion is worrying and the results from these pipelines require further investigation, in order to check whether this behavior introduces any systematic errors.

The catalog presented here is publicly available at the LAMOST<sup>11</sup> and CDS<sup>12</sup> websites. In future we would like to extend the catalog to more recent (and larger) LAMOST data releases, using a new version of SP\_Ace designed to overcome the limitations identified in this current study.

This work was supported by the National Key Basic Research Program of China “973 Program” 2014 CB845700 & CB845702, and by the National Natural Science Foundation of China (NSFC) under grants 11673083 (PI: M.C. Smith), 11333003 (PI: Shude Mao) & 11373054 (PI: L. Chen).

C.B. and E.K.G. were supported by Sonderforschungsbereich SFB 881 “The Milky Way System” (sub-project A5) of the German Research Foundation (DFG). D.S. is the recipient of an Australian Research Council Future Fellowship (project number FT1400147).

Guoshoujing Telescope (the Large Sky Area Multi-Object Fiber Spectroscopic Telescope, LAMOST) is a National Major Scientific Project built by the Chinese Academy of Sciences. Funding for the project has been provided by the National Development and Reform Commission. LAMOST is operated and managed by the National Astronomical Observatories, Chinese Academy of Sciences.

## APPENDIX

### IDENTIFIED PROBLEMS IN SP\_ACE

During the progress of this work we found one bug in the LAMOST version of SP\_Ace that affects the mechanism with which SP\_Ace aborts the analysis of spectra with large RV. This involves the offset limit in radial velocity correction beyond which SP\_Ace stops, and affects the LAMOST version only (the official public version of SP\_Ace does not have this bug). Since the LAMOST version of SP\_Ace handles both the blue and the red part of the spectrum, SP\_Ace stops when one or both parts show a wavelength offset (due to the RV) larger than  $1.27\text{FWHM}$ . For this comparison,

<sup>11</sup> <http://dr1.lamost.org/doc/vac>

<sup>12</sup> <http://cds.u-strasbg.fr>



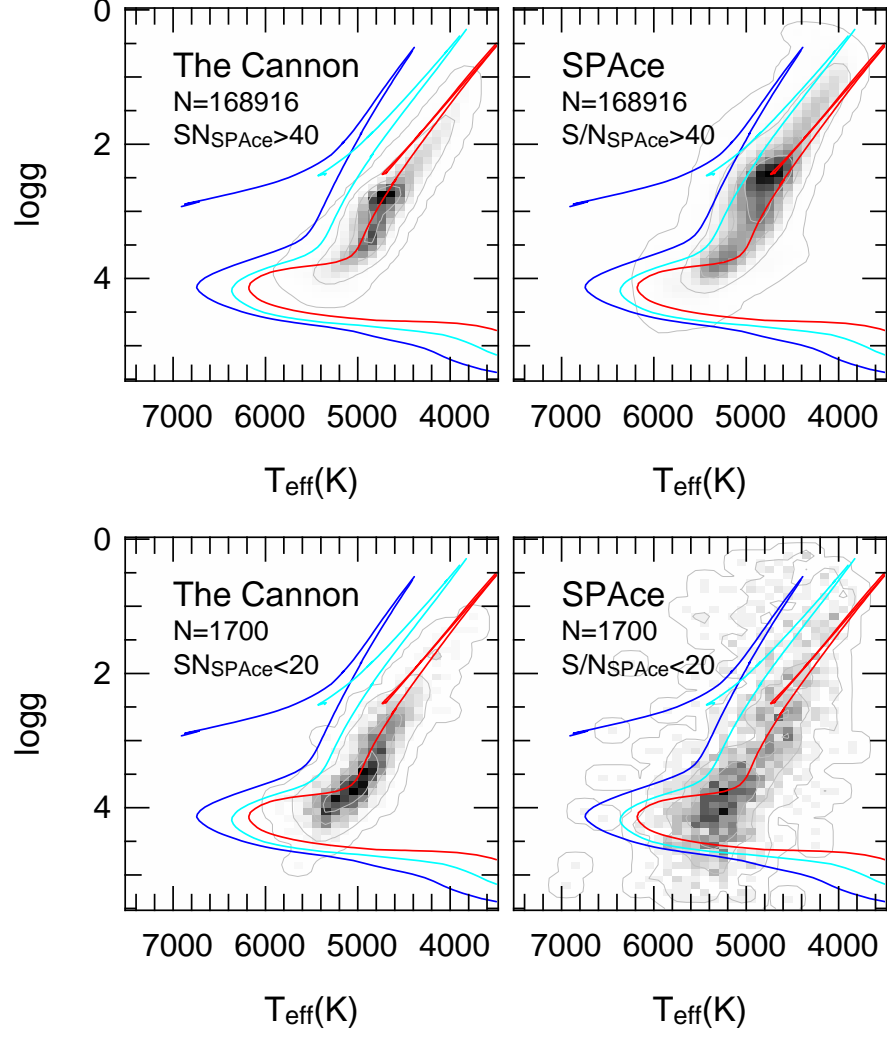


**Figure 15.** Density distribution of the LAMOST spectra in the  $(T_{\text{eff}}, \log g)$  plane for *The Cannon* (left panel) and SP\_Ace (right panel) for stars with  $S/N_{\text{SPACe}} > 40$  (top) and  $S/N_{\text{SPACe}} < 20$  (bottom). The red, light blue, and blue lines represent the same isochrones as in Fig. 4.

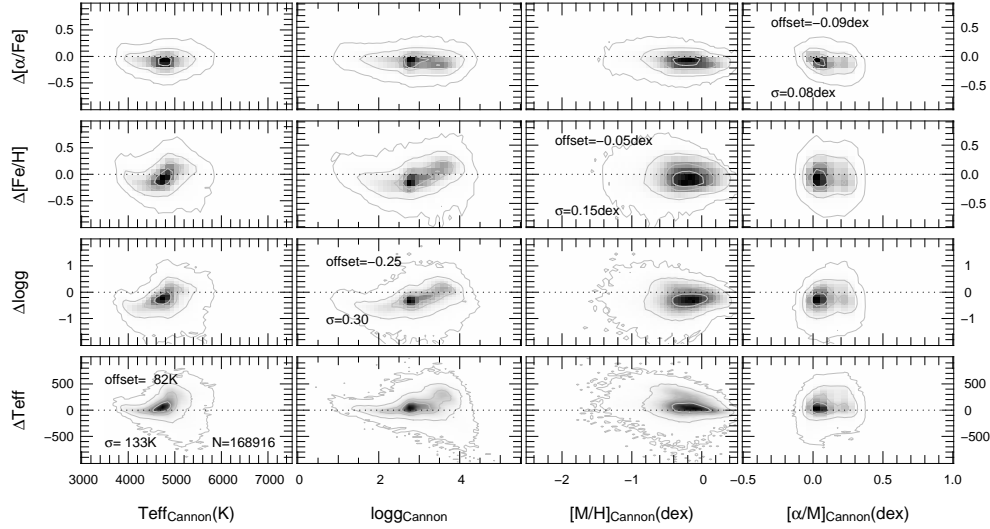


**Figure 16.** Residuals (SP\_Ace minus *The Cannon*) of the stellar parameters with respect to the *The Cannon* values for stars with  $S/N_{\text{SPACe}} > 40$ .

the source code translates the RV into  $\text{\AA}$  at the wavelength of  $5500\text{\AA}$  for both blue and red parts. This is a mistake because in this way the blue and red RV limits at which SP\_Ace stops are different, with the blue part giving the more stringent limit (which is  $\sim \pm 200\text{km s}^{-1}$  for an average  $\text{FWHM}_b \sim 2.9\text{\AA}$ ). However it must be stressed that, even if this bug were not present, the blue and red RV limits can never be constant because the limit depends on the  $\text{FWHM}_b$  and  $\text{FWHM}_r$ , which are not equal within one spectrum, nor among different spectra. This does not affect the robustness of any of the parameters derived by SP\_Ace but it can create a bias against stars with high radial velocity (with respect to the LSR). This will be corrected in our next version of LAMOST SP\_Ace.

#### VALIDATION PLOTS

For the sake of completeness, here we include additional plots illustrating the comparison between SP\_Ace and the reference data sets described in Section 4. These plots show the detailed correlations between parameters and are helpful in identifying potential problems with SP\_Ace parameters.

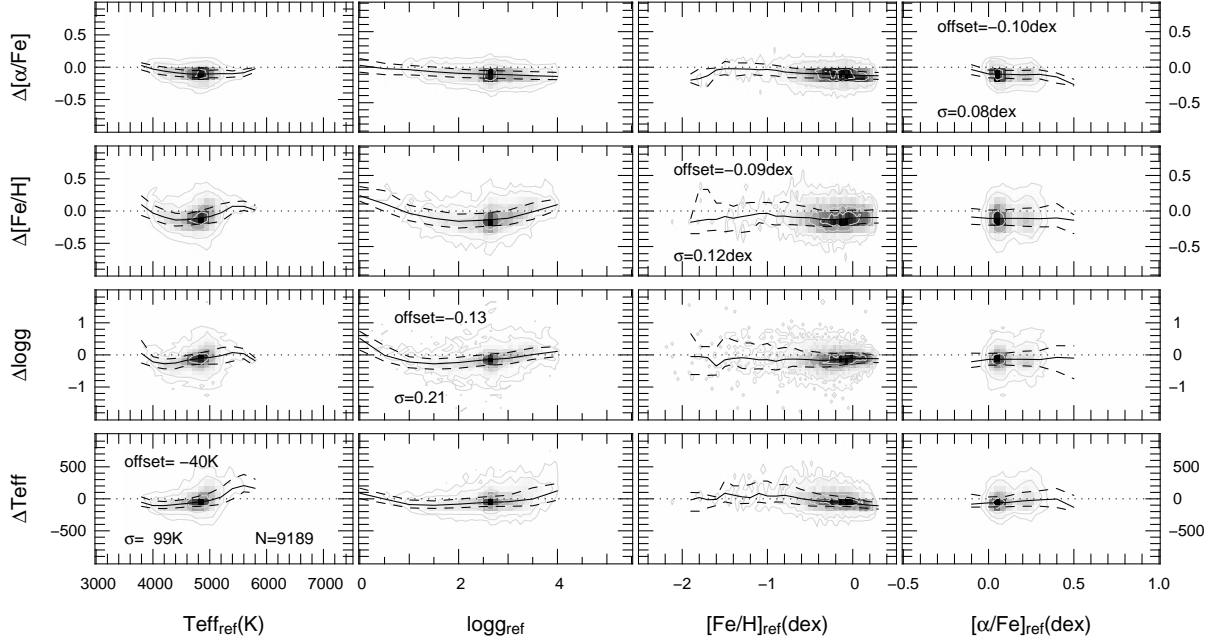


**Figure 17.** Residuals (SP\_Ace minus ASPCAP/APOGEE) of the stellar parameters with respect to the reference parameters for stars with  $S/N_{\text{SP\_Ace}} > 40$ . The solid black lines show the median of the residuals as a function of the reference stellar parameter, while the upper and lower dashed lines denote the interval holding 68% of the sample. These have been constructed using bins of width 200 K in  $T_{\text{eff}}$ , 0.5 in  $\log g$ , 0.1 dex in  $[\text{M}/\text{H}]$  and  $[\alpha/\text{Fe}]$ .

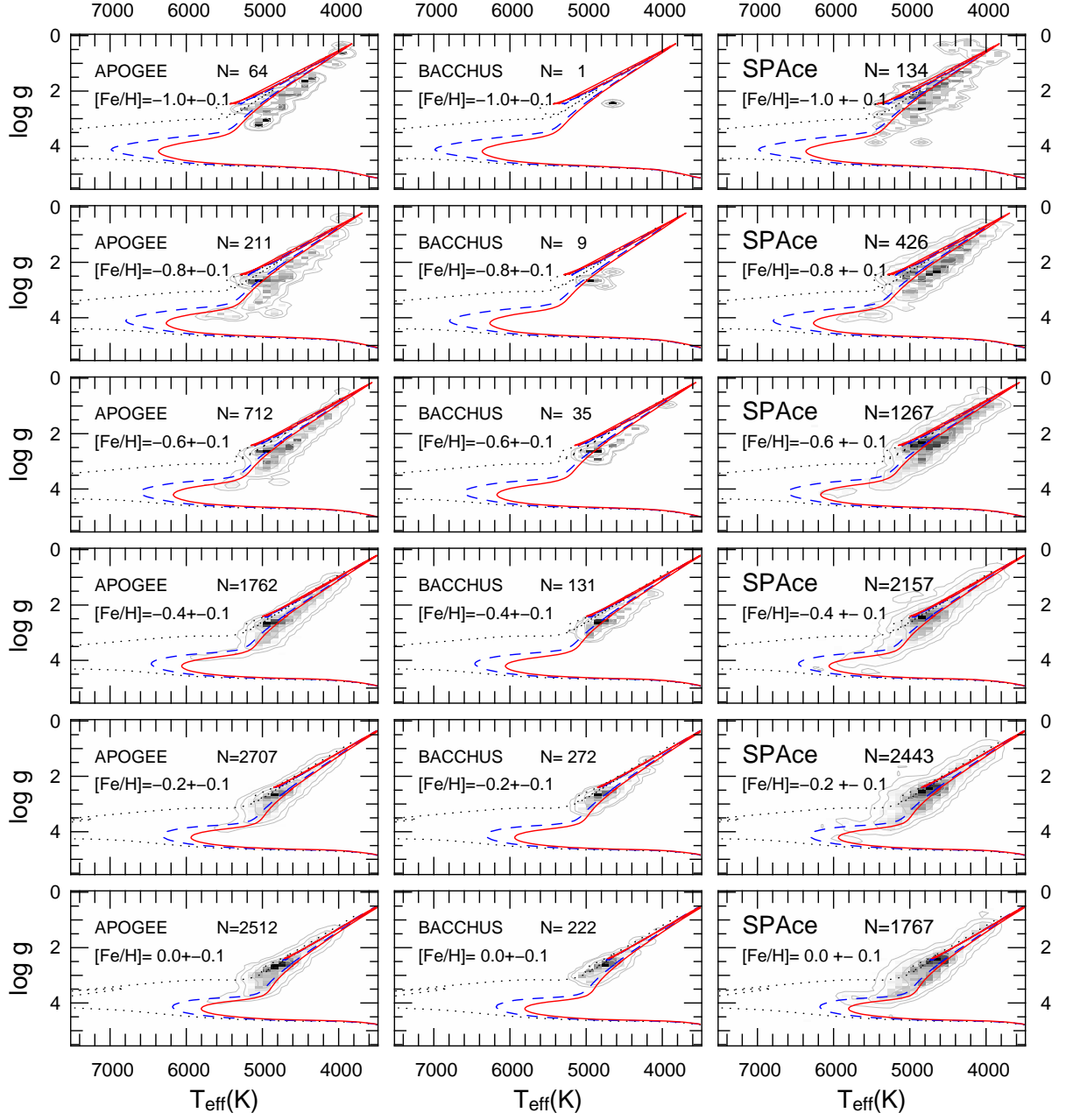


**Figure 18.** Distribution of stars in the  $(T_{\text{eff}}, \log g)$ -plane for the APOGEE/ASPCAP, BACCHUS, and SP\_Ace samples, divided into bins of  $[\text{Fe}/\text{H}]$  with half-width of 0.1 dex. The average  $[\text{Fe}/\text{H}]$  of the bins increases from top to bottom. The dotted black, blue dashed, and solid red lines are Bressan et al. isochrones of 1, 5 and 10 Gyr, respectively, with metallicity corresponding to the  $[\text{Fe}/\text{H}]$  bin. The stars included here have  $S/N_{\text{SP_Ace}} > 40$ . The grey-scale indicates the relative density of stars and the contours enclose 34, 68, 95, and 99% of the sample.

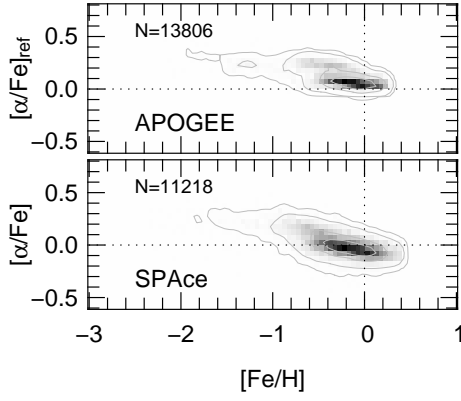


**Figure 19.**  $\alpha/\text{Fe}$  distributions for APOGEE stars with spectra also observed by LAMOST (and for which  $S/N_{\text{SP\_Ace}} > 40$ ). The top panel shows the ASPCAP parameters from the APOGEE spectra, while the bottom panel shows the SP\_Ace parameters from the LAMOST spectra.

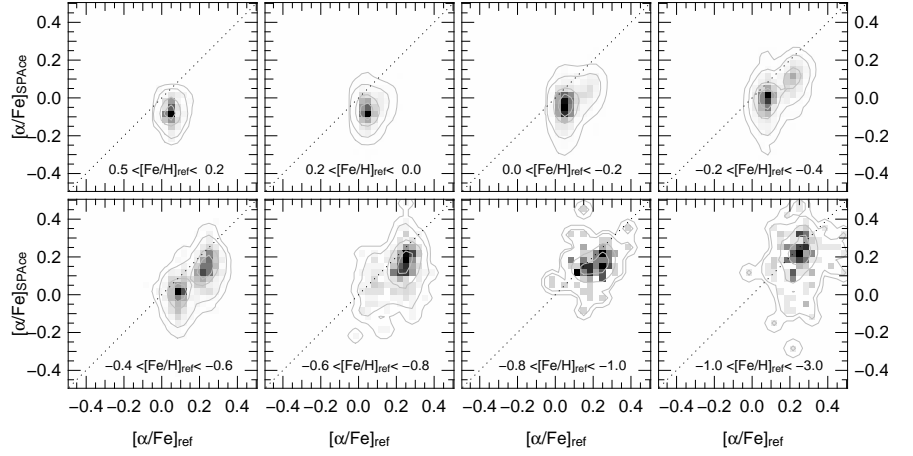


**Figure 20.** Comparison between  $\alpha/\text{Fe}$  derived by ASPCAP and SP\_Ace, divided in ASPCAP  $[\text{Fe}/\text{H}]$  bins, for stars with  $S/N_{\text{SP\_Ace}} > 40$ .

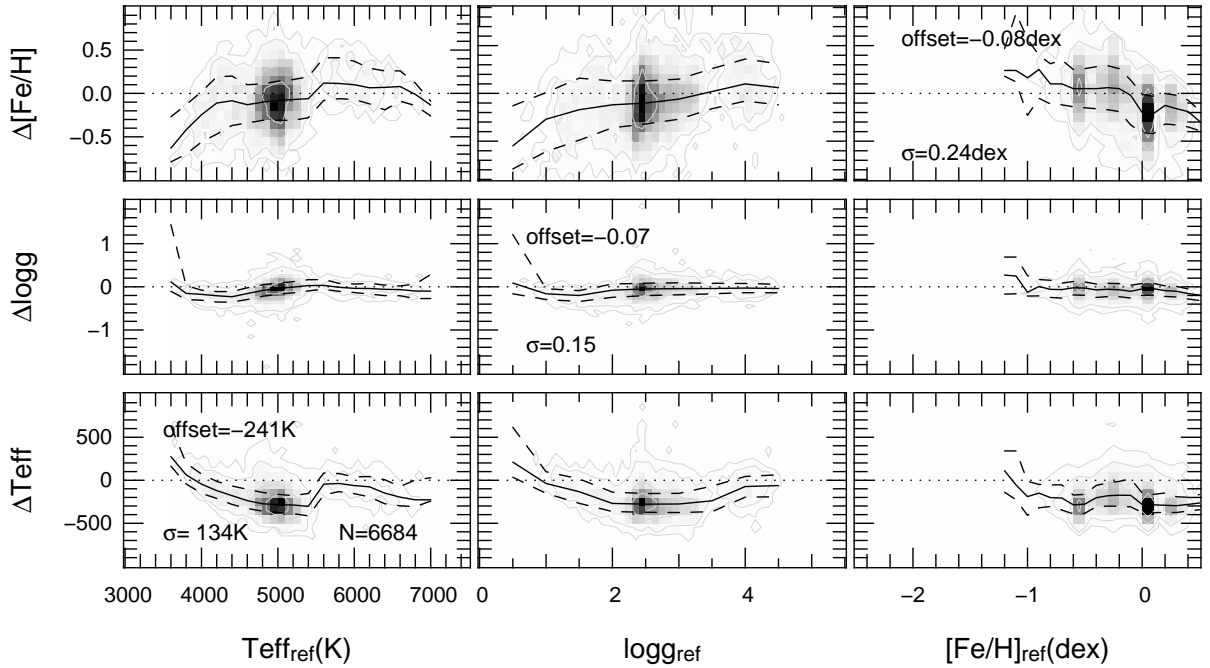


**Figure 21.** Residuals (SP\_Ace minus the Kepler stars of Huber et al.) of the stellar parameters with respect to the reference parameters for stars with  $S/N_{\text{SP\_Ace}} > 40$ . Black and dashed lines as in Fig. 17.



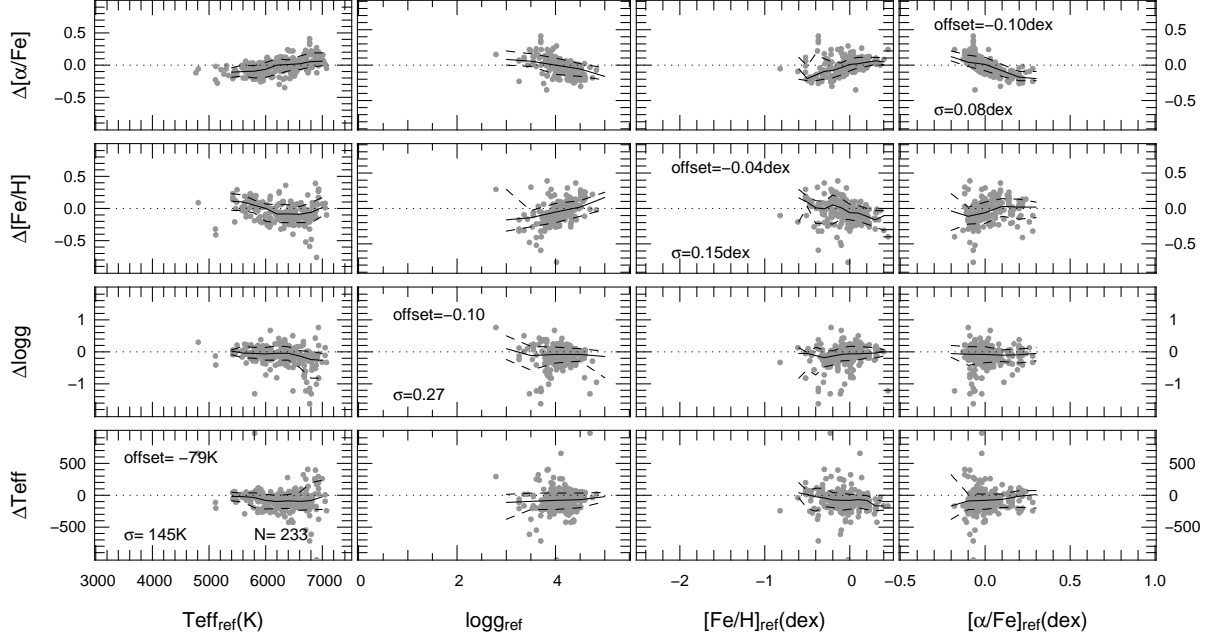


**Figure 22.** Residuals (SP\_Ace minus Casagrande et al.) of the stellar parameters with respect to the reference parameters for stars with  $S/N_{\text{SPAce}} > 40$ . Black and dashed lines as in Fig. 17.

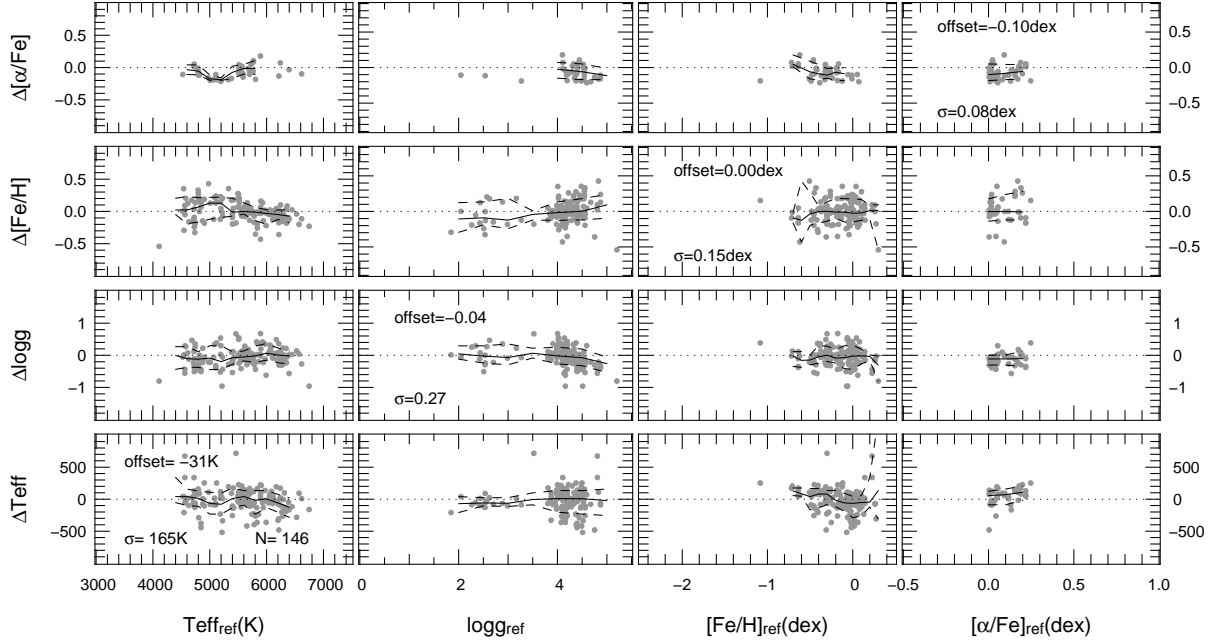


**Figure 23.** Residuals (SP\_Ace minus GES) of the stellar parameters with respect to the reference parameters for stars with  $S/N_{\text{SPAce}} > 40$ . Black and dashed lines as in Fig. 17.

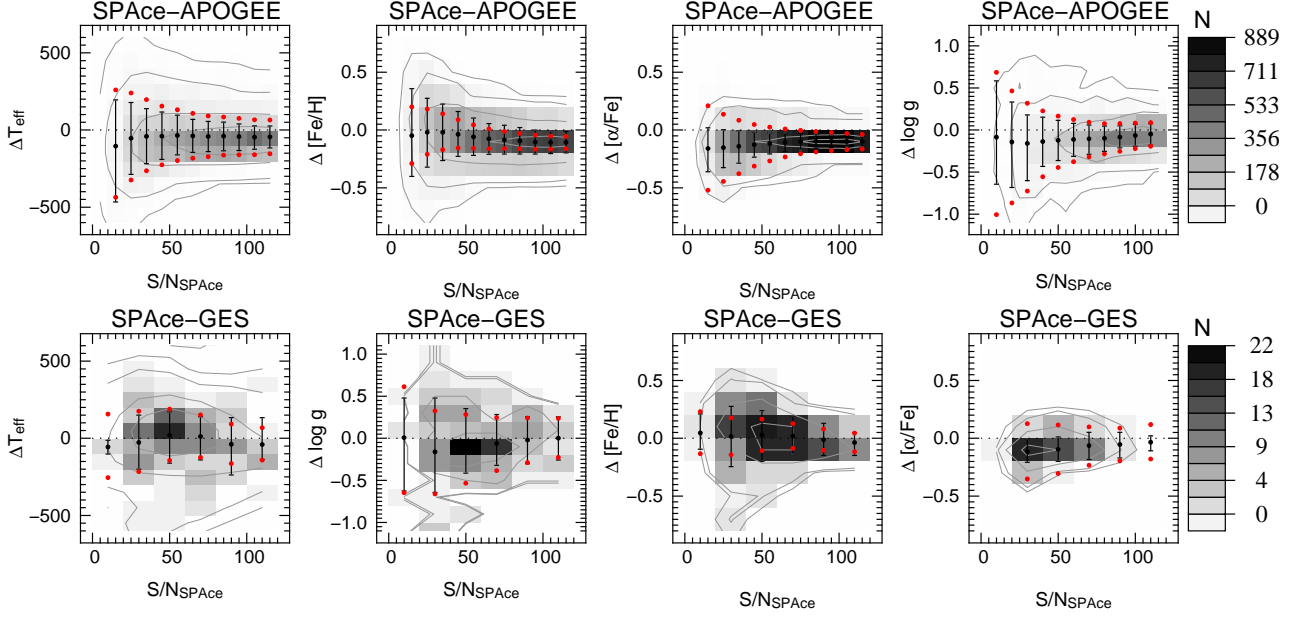


**Figure 24. Top:** Density distributions for the discrepancies (SP\_Ace minus reference) for data sets dominated by giant stars. The left and middle panels show the comparison of SP\_Ace and ASPCAP/APOGEE, while the right panel shows SP\_Ace compared with the Kepler stars of Huber et al. The dots with error bars represent the average discrepancy and  $1\sigma$  of the distribution for each bin in  $S/N_{\text{SP\_Ace}}$ , while the red dots represent the average uncertainties ( $\pm 1\sigma$ ) computed by adding the SP\_Ace and reference errors in quadrature. The grey-scale indicates the density of points per pixel (see bar on right), while the contours enclose 34, 68, 95, and 99% of the sample and all stars have  $S/N_{\text{SP\_Ace}} > 40$ . **Bottom:** Density distributions for the discrepancies between SP\_Ace and GES, i.e., for a sample dominated by main-sequence stars. Symbols, grey-scale bar, and contours are as in the top panel.

## REFERENCES

- Allende Prieto, C., Majewski, S. R., Schiavon, R., et al. 2008, *Astronomische Nachrichten*, 329, 1018
- Allende Prieto, C., Beers, T. C., Wilhelm, R., et al. 2006, *ApJ*, 636, 804
- Boeche, C., & Grebel, E. K. 2016, *A&A*, 587, A2
- Bedding, T. R., Mosser, B., Huber, D., et al. 2011, *Nature*, 471, 608
- Bressan, A., Marigo, P., Girardi, L., et al. 2012, *MNRAS*, 427, 127
- Bruce, S. F., Higinbotham, J., Marshall, I., & Beswick, P.H., 2000, *JMagR*, 142, 57
- Casagrande, L., Schönrich, R., Asplund, M., et al. 2011, *A&A*, 530, A138
- Castelli, F., Kurucz, R. L., 2003, in *IAUS symp. 210, Modelling of Stellar Atmospheres*, ed. N. Piskunov, W.W. Wiess and D.F. Gray, Published on behalf of the IAU by the ASP, 20
- Cui, X.-Q., Zhao, Y.-H.; Chu, Y.-Q., et al. 2012, *RAA*, 12, 1197
- Dalton, G., Trager, S. C., Abrams, D. C., et al. 2012, *Proc. SPIE*, 8446, 84460P
- de Jong, R. S., Bellido-Tirado, O., Chiappini, C., et al. 2012, *Proc. SPIE*, 8446, 84460T
- Deng, L.-C., Newberg, H.J., Liu, C., et al. 2012, *RAA*, 12, 735
- Dong, S., Zheng, Z., Zhu, Z., et al. 2014, *ApJ*, 789, 3
- García Pérez, A. E., Allende Prieto, C., Holtzman, J. A., et al. 2016, *AJ*, 151, 144
- Gilmore, G., Randich, S., Asplund, M., et al. 2012, *The Messenger*, 147, 25
- Gray, R. O., & Corbally, C. J. 1994, *AJ*, 107, 742
- Hawkins, K., Masseron, T., Jofré, P., et al. 2016, *A&A*, 594, A43
- Ho, A. Y. Q., Ness, M. K., Hogg, D. W., et al. 2017, *ApJ*, 836, 5
- Ho, A. Y. Q., Rix, H.W., Ness, M. K., et al., 2017, *ApJ*, 841, 40
- Holtzman, J. A., Shetrone, M., Johnson, J. A., et al. 2015, *AJ*, 150, 148
- Huber, D., Silva Aguirre, V., Matthews, J. M., et al. 2014, *ApJS*, 211, 2
- Koleva, M., Prugniel, P., Bouchard, A., & Wu, Y. 2009, *A&A*, 501, 1269
- Liu, C., Fang, M., Wu, Y., et al. 2015, *ApJ*, 807, 4
- Luo, A.-L., Zhao, Y.-H., Zhao, G., et al. 2015, *Research in Astronomy and Astrophysics*, 15, 1095
- Magrini, L., Randich, S., Friel, E., et al. 2013, *A&A*, 558, A38
- Mucciarelli, A., Pancino, E., Lovisi, L., Ferraro, F. R., & Lapenna, E. 2013, *ApJ*, 766, 78
- Mészáros, S., Holtzman, J., García Pérez, A. E., et al. 2013, *AJ*, 146, 133
- Ness, M., Hogg, D. W., Rix, H.-W., Ho, A. Y. Q., & Zasowski, G. 2015, *ApJ*, 808, 16
- Nordström, B., Mayor, M., Andersen, J., et al., 2004, *A&A* 418, 989
- Pinsonneault, M. H., Elsworth, Y., Epstein, C., et al. 2014, *ApJS*, 215, 19
- Prugniel, P., Soubiran, C., Koleva, M., & Le Borgne, D. 2007, *VizieR Online Data Catalog*, 3251, 0
- Steinmetz, M., Zwitter, T., Siebert, A., et al. 2006, *AJ*, 132, 1645
- Recio-Blanco, A., Bijaoui, A., & de Laverny, P. 2006, *MNRAS*, 370, 141
- Salaris, M., Chieffi, A., Straniero, O., 1993, *AJ*, 414, 580
- Snedden, C., PhD theses, Univ. Texas at Austin
- Stello, D., Huber, D., Bedding, T. R., et al. 2013, *ApJL*, 765, L41
- Tian, H.-J., Liu, C., Carlin, J. L., et al. 2014, *ApJ*, 809, 145
- Xiang, M. S., Liu, X. W., Yuan, H. B., et al. 2015, *MNRAS*, 448, 822
- Xiang, M.-S., Liu, X.-W., Shi, J.-R., et al. 2017, *MNRAS*, 464, 3657
- Yanny, B., Rockosi, C., Newberg, H. J., et al. 2009, *AJ*, 137, 4377
- Wu, Y., Luo, A.-L., Li, H.-N., et al. 2011, *Research in Astronomy and Astrophysics*, 11, 924
- Zucker, D. B., de Silva, G., Freeman, K., Bland-Hawthorn, J., & Hermes Team 2012, *Galactic Archaeology: Near-Field Cosmology and the Formation of the Milky Way*, 458, 421